CZECH TECHNICAL UNIVERSITY IN PRAGUE

FACULTY OF MECHANICAL ENGINEERING
DEPARTMENT OF ENERGY ENGINEERING

Dissertation

Accumulation of heat in basalt at high temperatures in packed and fluidized bed

Ing. Karin Astrid Senta Rindt

Doctoral study programme: Energy and Process Engineering

Prague, May 2022

Supervisor:
prof. Ing. František Hrdlička, CSc.
Department of Energy Engineering
Faculty of Mechanical Engineering
Czech Technical University in Prague
Technická 4
166 07 Prague 6
Czech Republic

Specialist Supervisor:
Ing. Lukáš Pilař, Ph.D.
Department of Energy Engineering
Faculty of Mechanical Engineering
Czech Technical University in Prague
Technická 4
166 07 Prague 6
Czech Republic

Anotace

Tato disertační práce seznamuje s možnosti akumulace tepla v čediči při vysokých teplotách v pevné a fluidní vrstvě. Cílem práce je seznámit s novou, relevantní možností ukládaní tepla pro Carnotovy baterie. Carnotova baterie je koncept skladovaní tepelné energie, který nabízí možnost ukládat energii, zejména z obnovitelných zdrojů energie, a podporuje tak cestu k udržitelnější energetické budoucnosti. V této prací je v rozsáhlém literárním přehledu uveden úvod do Carnotových baterií a skladování tepelné energie. V prací jsou diskutovaný různé druhy materiály pro ukládání teplené energie a technologie s uvedením důvodu, proč je čedičová hornina obzvláště zajímavá pro skladovaní energie. Přírodní čedič a litý čedičový produkt jsou analyzovaný z hlediska jejich vhodnosti a chování jako materiálu akumulujícího energii až do $750°C$.

Hlavní přínosy práce jsou zejména následující:

1. Experimenty a matematický model rychlosti dosažení plné potenciální tepelné kapacity přírodního a litého čediče k popisu chování při nabíjení a vybíjení přírodního a litého čediče pro použití při akumulaci tepelné energie.

2. Hodnocení objemových, hustotních a povrchových změn přírodního a litého čediče vlivem cyklování (nabíjení a vybíjení, tj. ohřev a ochlazování materiálu).

3. Porovnání chování při skladování v náplni a ve fluidním loži na základě experimentálních studií s pískem a návrh vícevrstvého skladování ve fluidním loži nabízející specifické teplotní gradienty podle potřeby aplikace.

Dalšími příspěvky autora do výzkumné oblasti, které nepřímo souvisí s hlavním tématem práce, jsou koncept sCO_2 Carnotova uspořádání baterie [KR1] a přehled probíhajících projektů baterií Carnot, které jsou podkapitoly ve „white paper“ o průmyslovém skladování tepelné energie EERA JP EEIP [KR2].

Klíčová slova: Carnotova baterie, akumulace tepelné energie, power-to-heat-to-power (P2H2P), pevná vrstvá, fluidní vrstvá, pevné akumulační materiály, čedič.

Abstract

This dissertation thesis exhibits possibilities for accumulating heat in basalt at high temperatures in a packed and fluidized bed. The goal is to offer a new, relevant thermal storage possibility for Carnot batteries. A Carnot battery is a thermal energy storage concept, offering the possibility to store energy, particularly from renewable energy sources, supporting the way to a more sustainable future. In this thesis, an introduction to Carnot batteries and thermal energy storage is given in an extensive literature review. Different storage materials and technologies are discussed, and the reason why basalt rock is an especially interesting storage material is given. Natural basalt and a cast basalt product are then analysed for their suitability and behaviour as energy storage material, focusing on high temperatures up to $750°C$.

In particular, the main contributions of the thesis are as follows:

1. Experiments and mathematical model of the speed of reaching the full potential heat capacity of natural and cast basalt to describe natural and cast basalts charging and discharging behaviour for the use in packed bed thermal energy storage.
2. Evaluation of volumetric, density and surface changes of the natural and cast basalt due to the influence of cycling (charging and discharging, i.e. heating and cooling, of the material).
3. Comparison of packed and fluidized bed storage behaviour, based on experimental studies with sand, and proposal of multi-layered fluidized bed storage, offering specific temperature gradients according to the need of an application.

Further contributions of the author to the research area, which are indirectly related to the main topic of the thesis, are the concept of a sCO_2 Carnot battery layout [KR1] and the overview of ongoing Carnot battery projects, which are sub-chapters in the white paper on industrial thermal energy storage of the EERA JP EEIP [KR2].

Keywords: Carnot battery, thermal energy storage (TES), power-to-heat-to-power (P2H2P), packed bed, fluidized bed, solid storage materials, basalt.

Affidavit

I hereby declare that the submitted thesis is my own work. I have only used the sources indicated and have not made unauthorised use of services of a third party. Where the work of others has been quoted or reproduced, the source is always given.

Karin Rindt Prague, 16.05.2022

Acknowledgements

First of all, I would like to express my gratitude to prof. Ing. František Hrdlička, CSc.for his supervision, funding acquisition, support and feedback.
My special thanks go to Ing. Lukáš Pilař, Ph.D.for his encouraging words, constant feedback and ongoing support with my ideas and goals.

Further, I would like to acknowledge the staff of the Department of Energy Engineering, in particular Petr Stříž, for his help in preparing the samples for the measurements and Ing. Pavel Skopec, PhD, for his help around the *mini-fluid*, as well as prof. Ing. Jan Hrdlička, Ph.D., prof. Ing. Michal Kolovratník, CSc. and Ing. Jana Novotná support and help with all organisational questions.
My research has been partially supported by the Grant Agency of the Czech Technical University in Prague, grant No. SGS20/116/OHK2/2T/12 and by the Technology Agency of the Czech Republic with the grant Moderní technologie pro akumulaci energie, grant No. TN01000007/10.

I would like to also thank prof. Ing. Milena Pavlíková, PhD and Ing. Adam Pivák from the Department of Material Engineering and Chemistry at the Faculty of Civil Engineering, as well as Ing. Zdeňka Jeníková, PhD from the Department of Materials Engineering of the Faculty of Mechanical Engineering, for the cooperation and support in some of my supplementary measurements,
My gratitude also goes to M. Sc. Bernd Eppinger from the Department of Chemical and Bioengineering at the Friedrich-Alexander-University of Erlangen-Nuernberg and M. Sc. Kai Knobloch from the Department of Energy Conversion and Storage at the Danish Technical University, for our cooperation and especially for all the great discussions and support we had for each other over the last years.

I would also like to thank my family and friends for their great support during this time. Finally, my greatest thanks go to my husband, Ing. Jan Rindt, for his infinite patience and care.

I was taught that the way of progress was neither swift nor easy.
Marie Curie

If we knew what it was we were doing, it would not be called research, would it?
Albert Einstein

Contents

List of Figures

List of Tables

Abbreviations and Symbols

Abbreviations

CHEST	Compressed Heat Energy Storage
CO_2	Carbon Dioxide
COP	Coefficient Of Performance
CSP	Concentrated Solar Power
DSC	Differential Scanning Calometry
ES	Energy storages
ETES	Electro-Thermal Energy Storage
HX	Heat Exchanger
LAES	Liquid Air Energy Storage
ORC	Organic Rankine Cycle
P2H2P	Power-to-Heat-to-Power
PCM	Phase Change Material
PHES	Pumped Heat Energy Storage
PHS	Pumped Hydro Storage
PTES	Pumped Thermal Energy Storage
TES	Thermal Energy Storage

Greek symbols

ε	Void fraction
η	Polytropic/isentropic efficiency
δ	Change in quantity
μ	Dynamic viscosity in $kg/(m * s)$
ρ	Density in kg/m^3
ϕ_s	Spericity of a particle

Symbols

a	Width of the mini-fluid in m
a	Crossflow area of the mini-fluid in m^2
b	Depth of the mini-fluid in m
c_p	Specific heat capacity at a constant pressure in $kJ/(kg * K)$
$d_p = d_{mean}$	Particle size (diameter) based on screen analysis in m
g	Gravity constant in m/s^2
m	Mass in kg
$\dot{m}$	Mass flow in kg/s
Q	Heat (capacity) in J or kWh
$\dot{q}$	Specific rate of heat flow in W/kg
$\dot{Q}$	Heat flow in $W = J/s$
R	Specific gas constant in $J/(kg * K)$
T	Temperature in K or $°C$
u	Superficial gas velocity in m/s
$\dot{V}$	Volume flow in m^3/h

Subscripts

ac	After cooling in the calorimeter
amb	Ambient
b	Basalt or bulk
bc	Before cooling in the calorimeter
cc	Charging cycle
comp	Compression
dc	Discharging cycle
exp	Expansion
f	Fluid
g	Gas
mf	Minimum fluidizing conditions
r	Rock
RT	Room temperature
s	Sand
st	Storage (or storage media)
w	Water
$x°C$	Temperatures to which rock patterns are heated
1,2,3,...	Cycle state points

Chapter 1

Introduction

With the increasing deployment of renewable energy sources, which naturally deliver energy intermittently, the need for energy storage is rising. A promising storage technology offering geographic independence and long storage duration is the concept of Carnot batteries.

1.1 Motivation - Renewable energy production and the resulting need for energy storage

The research area and specific goals of this work will be explained in this chapter.

1.1.1 Renewable Energy Sources

The Czech Republic reduced its CO_2 emissions by over 30 % since 1990, by an overall lower use of energy and greater employment of nuclear energy as well as renewable energies [12]. However, to fulfil the goals set in the European Green Deal [13], further action needs to be taken. A higher amount of energy will have to be retrieved from variable renewable energy sources (VRES), wind and sun in particular. Their natural intermittency causes a difference between energy production and need, which requires a shift of available energy via energy storage. The fluctuation of VRES further causes challenges in the electric grid and can be handled up to a maximum of 10 % VRES without any further changes [14].

1.1.2 Thermal Energy Storage

Energy storage (ES) plays an undeniable and important role on the way of decarbonising energy production [15]. [16] visualised the potential of different storage principles, rating electro-thermal energy storage (ETES) as technology feasible for longer storage time and higher power, as needed for combating the described VRES issues. A Carnot battery works according to the power-to-heat-to-power (P2H2P) principle (Fig 1.1). If the system employs a heat pump to store the energy, it is also called pumped thermal energy storage

(PTES) or pumped heat energy storage (PHES). PHES is easily confused with pumped hydro storage (PHS) and, therefore, is not recommended to be used. Currently, the most widely used notion is Carnot battery.

A Carnot Battery has three phases:

1. the charging phase, in which power is converted to heat,
2. the storage phase, in which heat is stored in hot (and cold) reservoirs,
3. the discharging phase, in which heat is converted back to power.

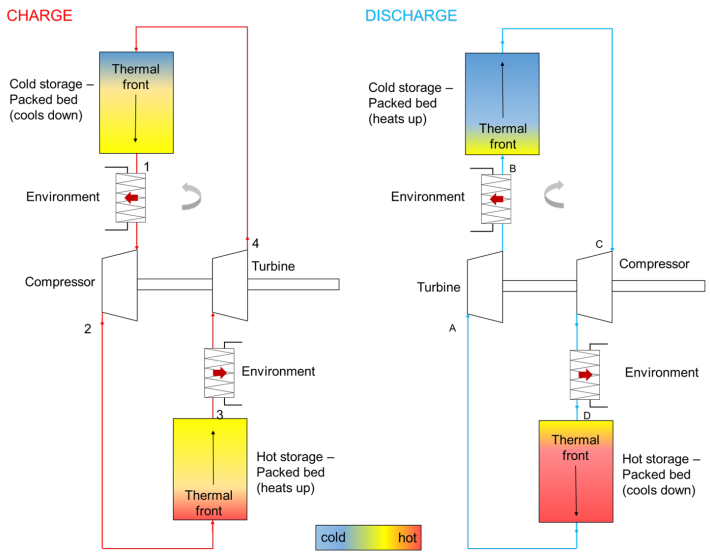

Figure 1.1: Carnot battery with packed bed storage and Brayton cycle for (dis)charging.

Because they play an important part in developing a greener future of energy production, Carnot batteries are the governing topic for this dissertation.

Chapter 2

State-of-the-Art of Carnot batteries

A Carnot battery has three main aspects: charging, storage and discharging. For every aspect and the combination of all three, there are numerous solutions. These shall be presented based on the current state-of-the-art in the following chapter.

2.1 Carnot battery layouts

This chapter shall briefly overview the different possibilities for charging and discharging Carnot batteries. Using an electric heater for charging a Carnot battery storage is probably the simplest way and can be combined with a steam or combined cycle for discharging. Other, more sophisticated system layouts with Brayton and Rankine cycles used as heat pump and power cycles are introduced to more detail. A summary of Carnot battery systems in the literature can be found in Table 2.1 on page 11.

2.1.1 Brayton cycle

A Brayton cycle operates above the critical point of a working fluid, which is therefore in a gaseous state throughout all processes. The T-s diagram of a simple Brayton Carnot battery storage system is shown in Fig. 2.1 and a recuperated Brayton cycle Carnot battery is shown in Fig. 2.2. Charging a Carnot battery with a simple Brayton cycle looks as follows:

- 1 to 2: compression of the gas
- 2 to 3: charging (heating up) the hot storage with the heat from the cycle heat by cooling down the gas + heat dissipation to the environment (3' to 3), to keep the storage vessels' outlet temperatures constant
- 3 to 4: expansion of the gas in a turbine
- 4 to 1: charging (cooling down) the cold storage while

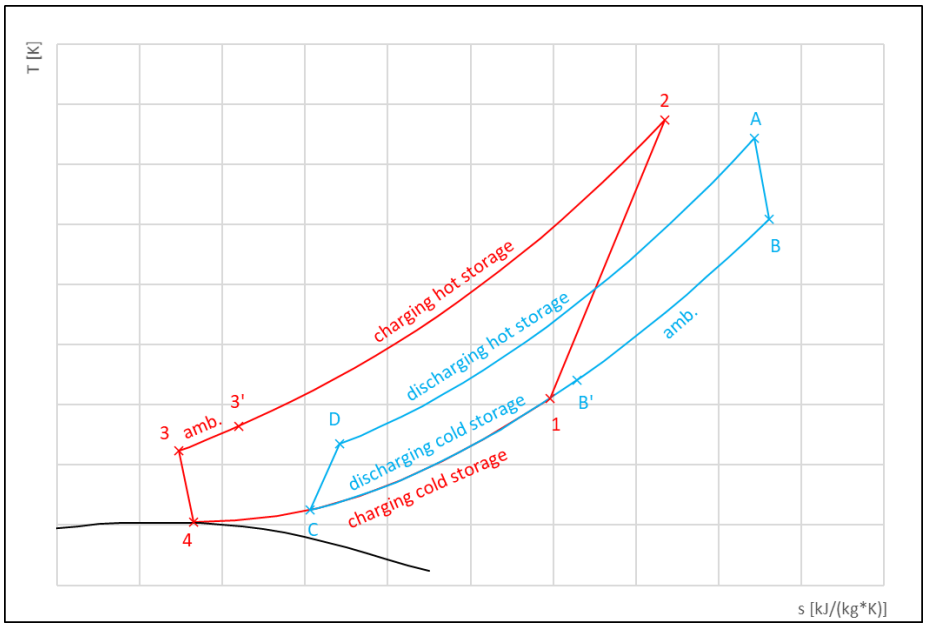

Figure 2.1: T-s-diagram: Carnot battery with (simple) Brayton cycle

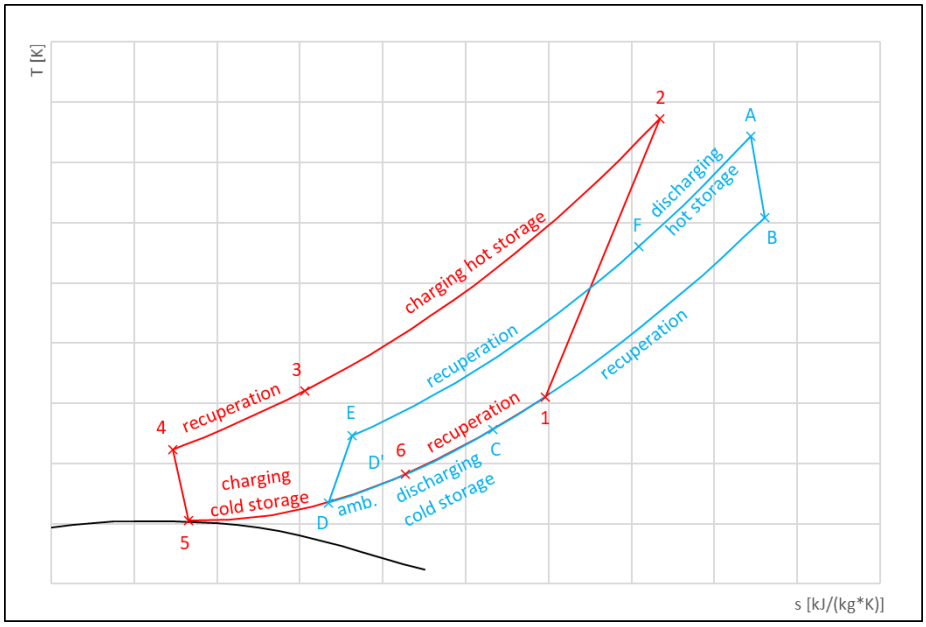

Figure 2.2: T-s-diagram: Carnot battery with recuperated Brayton cycle

Discharging a Carnot battery with a simple Brayton cycle:

- A to B: expansion of the gas in a turbine
- B to C: discharging (heating) the cold storage while cooling down the gas + heat dissipation to the environment (B to B')

– C to D: compression of the gas

– D to A: discharging (cooling) the hot storage by heating the gas

A Brayton cycle with a fluid two-tank storage (Fig. 2.6) employs heat exchangers on the place in the cycle where the packed beds would be integrated. The heat exchangers transfer the heat to or from a fluid flowing from one tank at a certain temperature to a second tank, which will then have at a different temperature. Because the heat transfer occurs between those two fixed temperatures, it will be constant, and there's no need for a heat exchanger after the storage to enforce this. However, one heat exchanger in the charging or discharging phase will still be necessary because of the irreversibilities within the cycle.

2.1.2 Rankine cycle

Rankine cycle Carnot battery can be split according to subcritical, transcritical Rankine cycles. Subcritical Rankine Carnot batteries usually have water or organic fluids (ORC) as the working fluid, transcritical Rankine Carnot batteries CO_2. In a Rankine cycle, the working fluid changes between gaseous (vapour) and liquid state. The layout of the Rankine cycle is similar to the ones for Brayton cycles, though a pump would be used for compression and expansion of the liquid fluid, also possible to be combined with packed bed (Fig. 2.7 and 2.8) and liquid storage tanks (Fig. 2.6). If a throttling device is used instead of a work-recovering expander, the energy through expansion is not usable. The general T-s-diagram for a subcritical Rankine cycle is shown in Fig. 2.3. Charging a subcritical Rankine cycle Carnot battery:

– 1 to 2: compression of the saturated vapour to superheated vapour

– 2 to 3: charging (heating) the hot storage with the heat from the cycle heat by cooling down (condensing) the working fluid until it reaches saturated liquid state

– 3 to 4: expansion of the gas in a pump in the liquid-vapour region

– 4 to 1: charging (cooling) the cold storage while heating the working fluid to saturated vapour state

Discharging a subcritical Rankine cycle Carnot battery:

– A to B: expansion of the vapour in a turbine

– B to C: discharging (heating) the cold storage while cooling down the working fluid until it reaches the state of saturated liquid

– C to D: compression of the liquid in a pump

– D to A: discharging (cooling) the hot storage by heating the working fluid (from liquid through liquid-vapour to vapour).

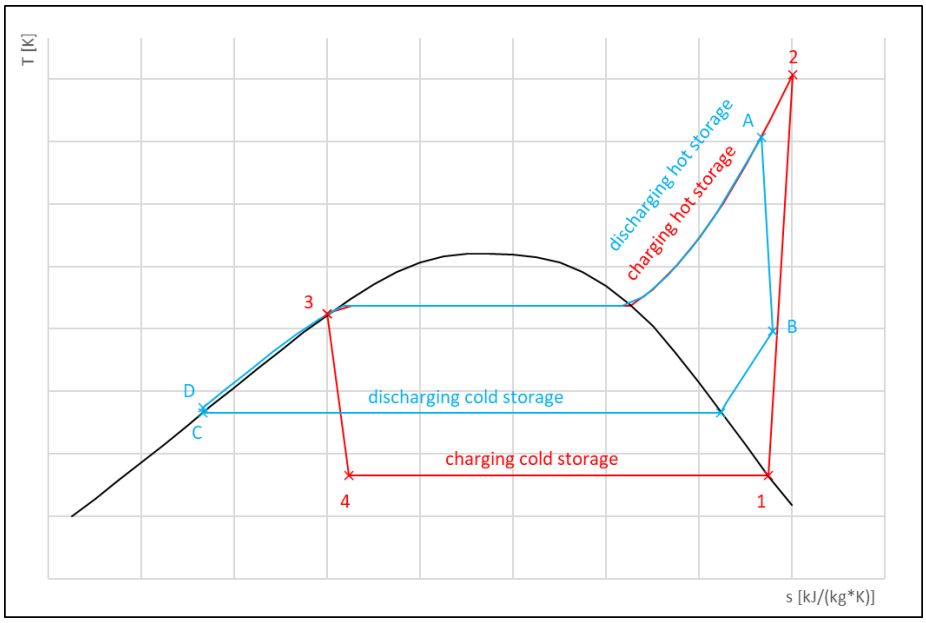

Figure 2.3: T-s-diagram of a (subcritical) Rankine Carnot battery

A transcritical CO_2 Rankine cycle is shown in Fig. 2.4. While the process differs from the subcritical Rankine cycle in so far, that the working fluid doesn't go through the liquid-vapour region while transferring heat transfer from and to the hot storage. The transcritical Rankine cycle can further be realised as an isothermal system (see Fig. 2.5).

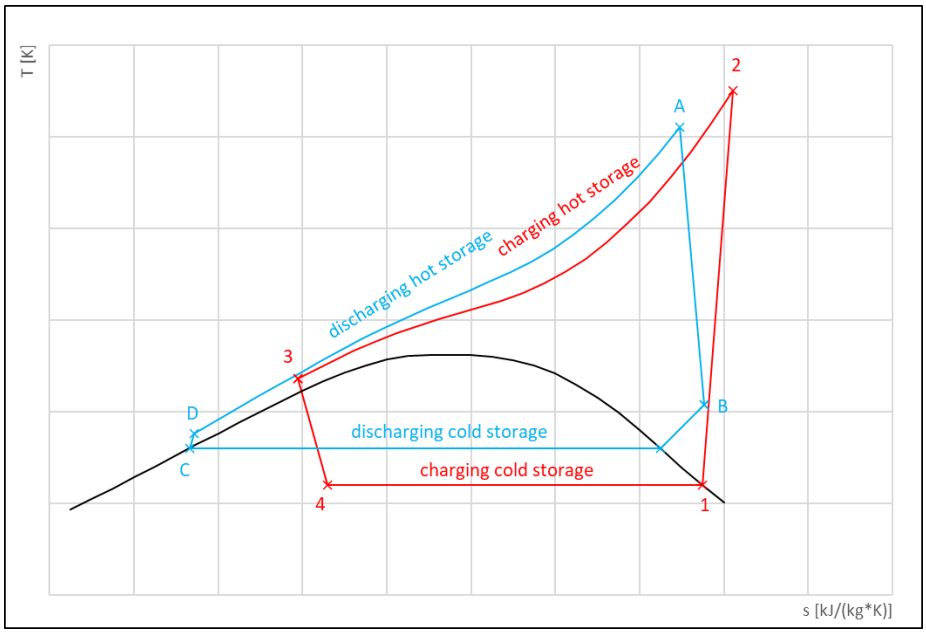

Figure 2.4: T-s-diagram of a transcritical Rankine Carnot battery

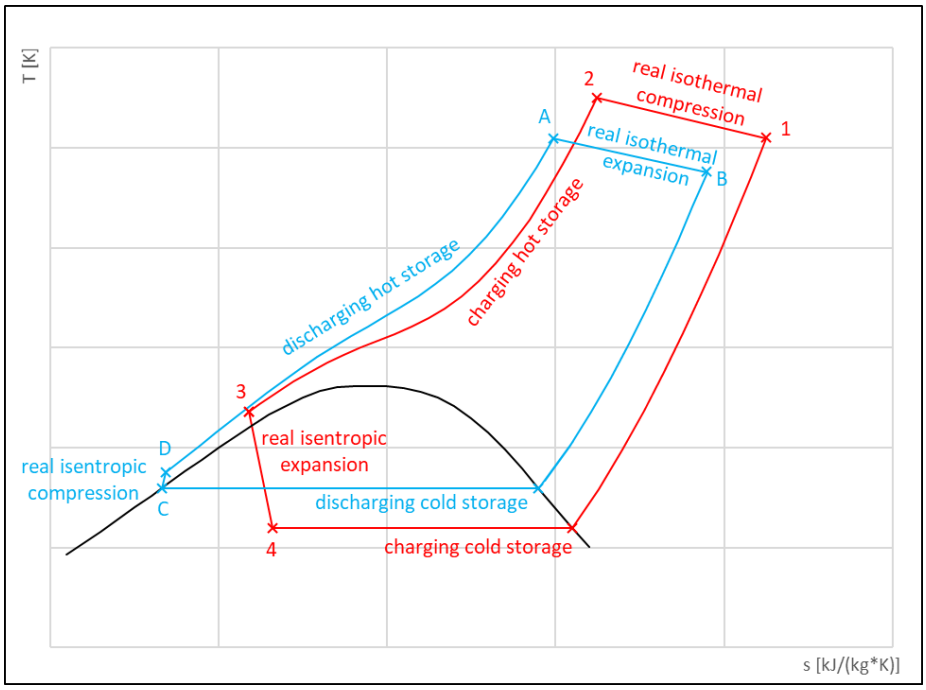

Figure 2.5: T-s-diagram of a transcritical isothermal Rankine Carnot battery

2.2 Thermal storage for Carnot batteries

Thermal storage can be classified into sensible, latent, or chemical storage, according to the storage material, and then further into active storage, where the storage media (direct) or a heat transfer fluid (indirect) is circulating, involving forced convection, and passive storage, where the storage material itself isn't flowing [17]. To describe the advantages and challenges and provide some basic calculation guidelines, the storage technologies in this chapter are split into passive packed bed and multi-tube storage and active liquid storage, which could have both latent and sensible storage material.

2.2.1 Active Storage

Active storage are widely used in CSP and tested in this context [17]. The storage material of active storage are liquids like water, molten salts, oil, etc., which can be directly or indirectly stored. The type of liquid storage employed in Carnot battery concepts is two-tank liquid storage with molten salt (also originally a concept from CSP plants, employed for Brayton PTES concepts) and pressurised water (so far mostly suggested for transcritical CO_2 Carnot batteries). As the name is already suggesting, the storage concept consists of two tanks filled with liquid storage material. One tank is filled with the storage material at the high temperature, and one tank is filled with the storage material at the low temperature. The temperature within the tanks is uniform. For heat transfer from the storage to the cycle, the fluid from the hot tank is pumped to the colder tank, passing a

heat exchanger through which the heat is transferred to the cycle, see Fig.2.6. It needs to be taken special care of that the maximum heat transfer from or to storage in charging and discharging phase is limited to the mass of fluid at a current state in those tanks. Losses

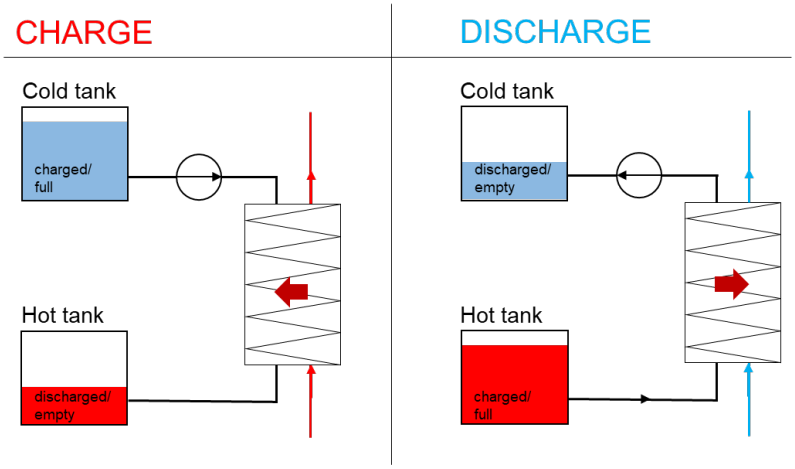

Figure 2.6: Scheme of the hot and cold two-tank storage system

in two-tank fluid storage are only due to self-discharge through the walls, maybe entropy generation due to movement inside the tank during filling and emptying and losses in the heat exchangers (pressure loss, irreversibilities in heat transfer). Another problem related to using heat exchangers is the pinch-point problem, which should be checked, especially for big differences in heat capacity between storage medium and cycle working fluid. For example, if the working fluid is supercritical CO_2, pinch-point problems can easily occur and limit the minimum temperature difference between cycle and storage medium.

2.2.2 Passive storage

For Brayton and Rankine cycles with hot and cold packed bed storage, the processes for charging and discharging are described in Fig. 2.7. Packed bed storage vessels are usually arranged vertically to comply with natural temperature stratification (see Fig. 2.8), though there are also a few investigations about horizontal storage. So, during the charging phase, the thermal front is moving down in the hot storage while heating it and is moving upwards in the cold storage while cooling it down. At the beginning of the discharging cycle, the material in the hot storage is at its high temperature, and the cold working fluid streaming through it from bottom to top pushes the thermal front upwards and cools down the storage. The charged state of the cold storage means it is at its low temperature. During the discharge phase, it supplies the cycle with the temperature sink while heating up (thermal front moving down).

Packed bed storage (Fig. 2.9, middle cut front view generally consists of a tank (storage vessel) which is packed with the storage material, e.g. pebbles, encapsulated PCM or other material. A cylinder-shaped vessel or cuboid tank can be often used. The storage material

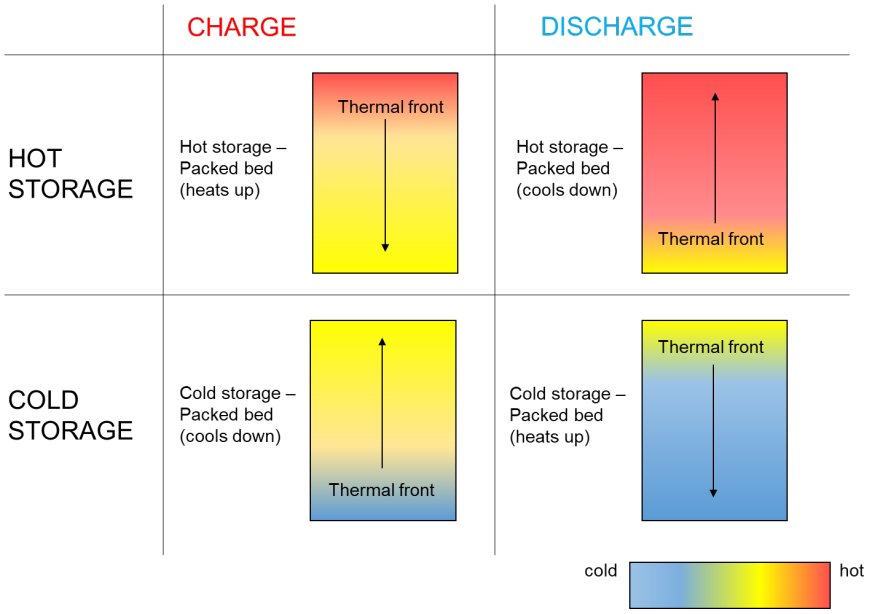

Figure 2.7: Scheme of a hot and cold packed bed storage

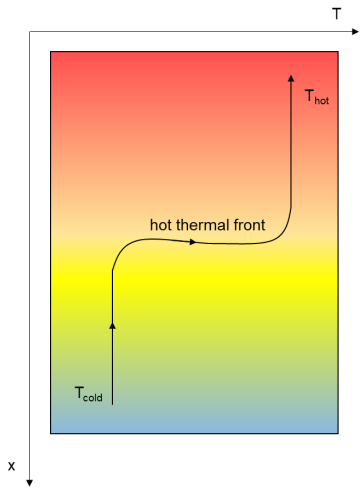

Figure 2.8: Scheme of vertical packed bed temperature stratification and thermal front

is loosely filled into the container so that the working fluid can pass through the spaces in between.

For a cycle with turbine and compressor, the mass flow can be simply set by the desired discharging time and power output (divided by the efficiency of the discharging cycle). It should be mentioned that in the packed bed of Brayton Carnot battery, the mass flow of the cycle and storage are the same, as the cycle fluid flows directly through it, which doesn't necessarily have to be like that, as a heat exchanger can be used between cycle and storage (as also for two-tank liquid storage). For the governing equations within a packed bed, the so-called Schumann model (based on work from Anzelius in 1926) is used, which

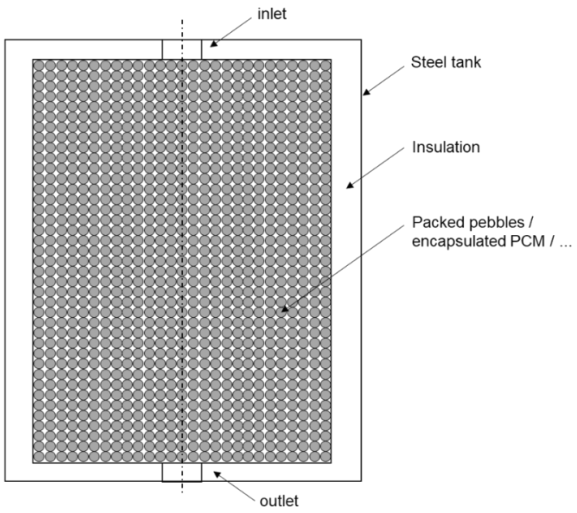

Figure 2.9: Schematic of vertical packed bed thermal storage

assumes a system to have [18]:

- Variation of solid and gas properties only in the z-direction (axis of the cylindrical storage vessel), as the packed bed diameter is much greater than the particle size and the insulation is efficient enough to have only small heat leakage and radial variation.
- Limited gas to solid heat transfer because of the small particle's thermal surface resistance.
- Conduction and heat leakage (longitudinally) occur from and through the solid.
- The gas flows kinetic and potential energy is neglected.

The aim is to balance pressure losses and thermal and conductive losses (increasing with steeper thermal fronts). Generally, radial-flow packed beds have lower pressure losses but higher thermal and conductive losses due to steeper thermal fronts [19]. A problem that should be mentioned in correlation with packed beds is the unbalanced mass flow due to steep thermal fronts, which come with great variation in temperature and density. Wang et al. [20] published an investigation about the unbalance of mass flow rate in Brayton Carnot batteries with packed bed reservoirs, with the result that the unbalanced mass flow of hot and cold reservoir and the closed cycle is between 0.26 % and 0.62 % (with experimental validation of a maximum variation to the predicted results of ± 8 %. The change in the total working fluid mass (0.36 % of the total mass flow over time) need to be stored in a buffer vessel, as already mentioned in chapter 2.1.1.

A horizontal packed bed for distributing thermal energy to a thermal oil plant was investigated by Odenthal et al. [21], finding no significant temperature satisfaction between top and bottom, even though the mass flow of the heat transfer fluid air was found to be up to 20 % higher in the centre than the mean bulk mas flow.

2.3 Summary of different Carnot battery layouts in the literature

The following Table 2.1 presents a summary of the different Carnot battery layouts which can be found in the literature.

Table 2.1: Summary of different Carnot battery layouts in the literature

Charging	Discharging	Hot storage	Cold Storage	Efficiency	Source
El. heater (air)	Combined cycle (air/water)	Direct, packed bed	N/A	41 % (48 % with extra combustion)	[22]
El. heater (solar salt 60 % NaNO3 + 40 % KNO3)	Rankine Cycle (water)	Direct, liquid, solar salt (one tank)	Direct, liquid, solar salt (one tank)	44 %	[23]
El. Heater (silicon)	Photovoltaics (glowing silicon)	Direct, liquid, silicon (one tank)	Direct, liquid silicon (one tank)	N/A	[24]
Brayton cycle (Argon)	Brayton cycle (Argon)	Direct, packed bed	Direct, packed bed	66.7 %	[25]
Brayton cycle (Argon)	Brayton cycle (Argon)	Direct, packed beds (several parallel)	Direct, packed beds (several parallel)	65.3 %	[26]
Brayton cycle (Argon)	Brayton cycle (Argon)	Indirect, packed beds, Nitrogen (several parallel)	Indirect, packed beds, Nitrogen (several parallel)	59.5 %	[26]
Brayton cycle with reciprocating devices (Argon)	Brayton cycle with reciprocating devices (Argon)	Direct, packed bed	Direct, packed bed	72 %	[27]
Brayton cycle with reciprocating devices (Argon)	Brayton cycle with reciprocating devices (Argon)	Direct, packed bed	Direct, packed bed	85 %	[28]
Brayton cycle with an extra electric heater (air)	Brayton cycle combined with ORC (air)	Direct, packed bed	Direct, packed bed	47,67 %.	[29]
Brayton cycle (high-temperature supercritical CO_2)	Brayton cycle (high-temperature supercritical CO_2)	Indirect, liquid, molten salt (two sets of two-tank storages)	Indirect, liquid, mineral oils or synthetic fluids (two-tank storage)	60.4 %	[30]

Charging	Discharging	Hot storage	Cold Storage	Efficiency	Source
Brayton cycle (low-temperature supercritical CO_2)	Brayton cycle (low-temperature supercritical CO_2)	Indirect, liquid, molten salt (two-tank storage)	Indirect, liquid, water (two-tank storage	78.4 %	[30]
Recuperated Brayton cycle (air)	Recuperated Brayton cycle (air)	Indirect, liquid, molten salt (two-tank storage)	Indirect, liquid, synthetic oil (two-tank storage)	55 %	[31]
Recuperated Brayton cycle with several stages of reheating and intercooling (air)	Recuperated Brayton cycle with several stages of reheating and intercooling (air)	Indirect, liquid, molten salt (two-tank storage)	Indirect, liquid, water (two-tank storage)	50 %	[31]
Brayton cycle with an extra electric heater (air)	Brayton cycle (air)	Direct, packed bed	Direct, packed bed	6.34 %	[3]
Brayton cycle with reciprocating devices (air) or waste heat from a combined cycle if used as bottoming cycle	Brayton cycle with reciprocating devices (air)	Indirect, concrete multi-tube, heat transfer material not specified	Indirect, ambient, air	52.3 % (24 % as bottoming cycle)	[32, 33]
Rankine cycle (propane)	Rankine cycle (propane)	Direct, packed bed	Direct, packed bed (latent storage, with glycol)	<50 %	[34]
Cascaded Rankine Cycle (ammonia and water)	Rankine Cycle (water)	Direct, packed beds (latent and sensible)	Indirect, ambient, air	N/A	[35]
Transcritical Rankine Cycle (CO_2)	Transcritical Rankine Cycle (CO_2)	Indirect, liquid, water (multi two-tank storage)	Indirect, liquid, salt-water eutectic	62 %	[31]

Charging	Discharging	Hot storage	Cold Storage	Efficiency	Source
Transcritical Rankine Cycle (CO_2)	Transcritical Rankine Cycle (CO_2)	Indirect, liquid, water (two-tank storage)	Indirect, water-ice (latent storage)	65 %, 51 % for 1 MW pilot	[36]
Transcritical Rankine Cycle (CO_2)	Transcritical Rankine Cycle (CO_2)	Direct, ground, bedrock	Indirect, water-ice (latent storage with extra chiller in charging mode)	45 %	[37]
Recuperated transcritical Rankine Cycle (CO_2)	Recuperated transcritical Rankine Cycle (CO_2)	Direct, ground, bedrock	Indirect, water-ice (latent storage with extra chiller in charging mode)	51 %	[37]
Transcritical Rankine Cycle (CO_2)	Transcritical Rankine Cycle with two-phase expansion (CO_2)	Direct, ground, bedrock (2 systems, high and low pressure)	Indirect, water-ice (latent storage with extra chiller in charging mode)	65 %	[37]
Transcritical isothermal Rankine Cycle (CO_2)	Transcritical isothermal Rankine Cycle (CO_2)	Indirect, liquid, water (double-acting liquid piston system with two storage tanks)	Indirect, water-ice (latent storage)	68.6 %	[38]
Transcritical Brayton Cycle with nuclear power high-temperature heat source (CO_2)	Transcritical Brayton Cycle (CO_2)	N/A	Indirect, water (two-tank storage)	44 %	[39]
Transcritical Rankine Cycle with nuclear power high-temperature heat source (CO_2)	Transcritical Rankine Cycle (CO_2)	Indirect, liquid, water (two-tank storage)	Indirect, water-ice (latent storage)	40.9 %	[39]

2.4 Carnot battery pilot plants and demonstrators

To complete the overview of Carnot batteries, this chapter adds a summary of the most relevant pilot plants and lab-scale demonstrators to the introduction.

SIEMENS Gamesa built a Carnot battery pilot plant in Hamburg-Altenwerder which went into operation in summer 2019 [40]. The Carnot battery uses an electric heater and blower to charge air as working fluid and a Rankine cycle for re-electrification. The bulk solid (packed bed) storage is filled with 1000 tonnes of volcanic rock and has a storage temperature of about $740°C$. The nominal power is 30 MW, while the electrical output power mainly depends on the Rankine cycle. Therefore, the maximum electrical output power is 1.5 MW. The storage capacity is 30 MWh electric (with a discharge time of 24h) and 130 MWh thermal energy. The overall system efficiency for power-to-heat-to-power is about 45% and 98 % for power-to-heat. SIEMENS Gamesa calls its concept ETES, in particular ETES:Base, ETES:Add and ETES:Switch. ETES:Base is a standalone Carnot battery system made for renewable energy solutions, providing electricity, heat or process steam with electricity as input. ETES:Add is supposed to provide heat for industrial processes such as fossil fuel power plants or other energy-intensive industrial plants. ETES:Switch should be used for repurposing fossil fuel power stations to energy storage plants by employing the existing turbomachinery. The retrofitting of coal power plants has increased in importance in Germany, and therefore for SIEMENS, because Germany's coal power plants will go offline until 2038 [41].

The Argon based **Carnot battery demonstrator of the Newcastle university** is standing at the Sir Joseph Swan Centre for Energy Research and was built with the help of the company Isentropic Ltd. It has 150 kW (600 kWh) and is as a 1 to 10 version of the concept by Howes [27] which has 2 MW (16 MWh). It operates between $-106°C$ and $500°C$, where the lower temperature is not as cold as the proposed $-166°C$. The round-trip efficiency reached with the demonstrator is about 60 % to 65% [42], which seems promising. However, the two reversible reciprocating devices necessary for the cycle are a high-cost factor [30]. Pictures of the demonstrator can be found online at [42] and [43].

Several **thermally integrated Carnot battery concepts** are being tested **in Liege, Belgium**. They utilise waste heat at $75°C$. The reversible heat pump/organic Rankine cycle operates between $15°C$ and $85°C$, reaching about 100 % power-to-heat-to-power efficiency (with COP of the heat pump of 14 and an ORC cycle efficiency of 7 %) [44].

In March 2018, **MAN Energy Solutions Schweiz AG and ABB Switzerland** started the development, production, and commercialization of a flexible Carnot battery system, which they call **three-way energy-management system** [45, 46]. Three-way system because it is capable of using, storing and distributing heat or cold and electricity simultaneously. The CO_2 transcritical Rankine cycle based Carnot battery offers a great range of configuration: 2 MW to 50 MW electrical input or output with a storage capacity of 10 MWh to over 100 MWh, and export of thermal heat between about $0°C$ and $120°C$ with a COP>6, depending on temperature level [47]. A 5 MW system, for example, would have a capacity of 30 MWh el., 110 MWh th. hot or 80 MWh th. cold [46]. The overall round-trip efficiency reached is 50-55 %, and up to 70 % with thermal integration

delivering hot or cold heat [45]. The MAN/ABB Carnot battery is operating at a maximum temperature of $119°C$ at 140 bar (gaseous CO_2) and a low-temperature of $-2,7°C$C at 32.4 bar [46]. It seems that MAN/ABB is using a transcritical CO_2 Rankine cycle. The cycle employs cascaded hot water storage, with four different temperature levels [45]. Three out of the four individually insulated tanks are at atmospheric pressure, and one is pressurised. As cold storage, they utilise a water-ice PCM tank. Every storage is coupled with the cycle via a heat exchanger. In the charging cycle, the CO_2 is compressed with a HOFIM™ turbo-compressor before heating the hot storage, followed by expansion and being pumped through the cold side of the cycle, cooling down the cold storage. In the discharging cycle, the CO_2 is expanded in a turbine, cooling down while heating up (melting the ice in) the cold storage, then compressed with the pump and heating up with the stored heat from the hot storage. A scheme of charging and discharging cycle is available online at [45]. The HOFIM™ turbo-compressor is hermetically sealed and developed by MAN to compress the CO_2 to its supercritical state at 140 bar and $120°C$. The theoretical concept of this storage developed at ABB was published by Mercangöz et al. [36] and further Morandin et al. [48].

The **Danish Technical University** in Lyngby has two thermal energy storage systems using diabase as storage material. The so-called ***shoe-box*** and the ***Droplet***. The cuboid *shoe-box* (Fig. 2.10a) is a 450 kW (th.) rock bed unit, used for tests up to $600°C$, at which it can deliver up to $460°C$ output temperature with a thermal efficiency of 69 % to 96 % [49–51]. The *Droplet* (Fig. 2.10b) is named after its droplet-like shape, caused by the combination of a conical frustum and hemispherical shaped housing [52]. The *Droplet* is underground storage with a volume of $3.2m^3$ (5394 kg total rock mass) and a storage capacity of 1 MWh (th.) [52]. The maximum round-trip efficiency is up to 80.7 %, at $675°C$, with a maximum thermal output of 58.06 kW [52]. They also analysed the degradation of the rock bed over 249 cycles (3458 hours of operation) [53].

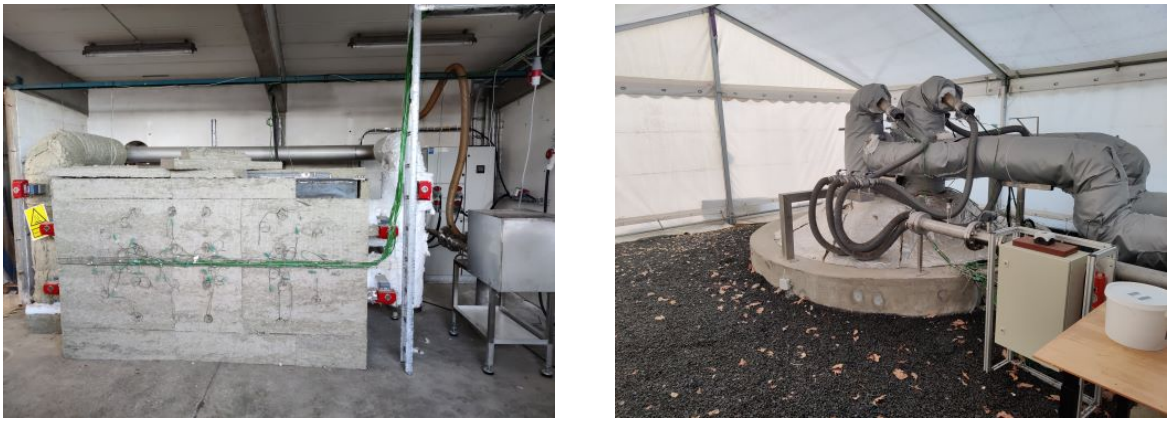

(a) *Shoe-box.* (b) Doplet.

Figure 2.10: TES at the Technical University of Denmark.

A project of Alphabet Inc's subsidiary X Development LLC (Moonshoot Technologies) started a project about cost-effective ES, which is now being continued by the **Malta Inc**.

The project is focused on a **Carnot battery with a Brayton air cycle** and a two-tank liquid storage system (the hot storage medium is molten salt and the cold storage medium is some chilled liquid [54–56]. The hot storage operates between $565°C$ and $290°C$ and the cold storage between ambient temperature ($20°C$) and $-65°C$ [57]. The company works on a 100 MW plant (1 GWh) and a 10 MW plant (80 MWh). Contractors of Malta Inc are developing a Plate & Frame Heat Exchanger for the heat transfer between cycle gas and storage fluid and the necessary turbomachinery.

2.5 Solid and liquid storage materials for thermal energy storage in Carnot batteries

This chapter gives an overview of possible storage materials for Carnot battery TES and the reason for choosing basalt to be investigated in this dissertation.

Gil et al. [17] and Alva et al. [58] offer an extensive overview of the properties of different sensible and latent storage materials (fluid and solid) and combinable storage tank materials. An overview and comparison of several packed bed materials in spherical form was done numerically by Benato and Stoppato [59], with the result that masonry has the shortest charging and discharging time, is relatively low cost and also has a low energy density. In contrast, copper has the highest energy density, is the most expensive and has the longest charging and discharging times. Other sensible materials are suggested by Fernandez et al. [60] and rated according to their thermal properties at temperatures between $150°C$ and $200°C$. Daschner et al. [61] experimentally analysed packed bed storage with the bulk materials up to $1200°C$ as a pebble regenerator for superheating in combined heat and power plants. Alumina Oxide, Quartz, Volcanic Rock and Basalt. Based on numerical and experimental studies ($600°C$, air as heat transfer fluid) it was found that sensible packed bed heat storage can obtain higher exergy recovery and energy density [62]. Shen et al. [63] conducted a study on temperature change and crack expansion of granite at high temperatures, using different cooling shock treatments with the result that the effect of macrocracking wasn't significant below $350°C$. Above $350°C$, the sample showed uniform microcracks around the injection hole, which became obvious above $550°C$. Grosu et al. [64] analysed different natural magnetite as packed bed storage material. Allen et al. [51, 65] chose diabase as material for their $1.5m^3$ big high-temperature TES (up to $600°C$). They propose basalt, diabase, and magnetite as the most promising rocks, resulting in rocks containing higher amounts of quartz and mica being less suited materials. The lab-scale TES was further introduced in section 2.4, together with the DTUs second lab-scale ground TES. Anderson et al. [66] emphasise the importance of using temperature-dependent thermophysical properties of storage material (in their case alumina) and heat transfer fluid (in their case air) for accurate results, which they calculated and experimentally tested for a packed bed TES between ambient and $120°C$.

Chapter 3

Problem Statement and Goal of Dissertation

The layout of the whole Carnot battery system, which means the combination of charging, storage, and discharging, is an important task for further study, as well as the research in the particular segments of it. Higher temperatures usually result in higher cycle efficiencies. Therefore, it is worth investigating possible Carnot battery layouts storing heat at high temperatures. The knowledge about cycles and heat pumps is quite extensive. However, the understanding of their combination in a Carnot battery and the storage itself is yet to be extended. The **aim** of this thesis is to extend the comprehension and variety of Carnot batteries and, with that, support society on its way to greener energy production. This leads to the following **goal** of this dissertation:

The goal of this dissertation is to gain objective knowledge for a potential hot storage using basalt rock. The results are applicable to energy storage concepts.

From the overall Carnot battery principle, the aspect of thermal storage, in particular the principle of a packed or fluidized bed thermal storage with basalt, was chosen to be investigated in this dissertation *Accumulation of heat in basalt at high temperatures in packed and fluidized bed*. Basalt is a natural rock, offering suitable thermal properties while having a low impact on nature and low price due to its high occurrence and wide availability. This makes it a viable and interesting candidate for Carnot battery systems.

The novelty of the proposed thermal energy storage system is its universal applicability for any Carnot battery system, i.e., any kind of heat pump and power cycle employing packed bed storage, using various heat transfer media. The approach in this dissertation thesis, the verified model of the storage behaviour, is necessary for the effective use of basalt as a storage material. For this, natural and cast basalt properties were experimentally examined in detail.

To reach this goal, the **objectives** and **tasks** with their respective **sub-goals**, were set as following:

1. Experiments and mathematical model of the speed of reaching the full potential heat capacity of natural and cast basalt
   - Charging and discharging behaviour of natural and cast basalt for the use in packed bed storage
   - Second life for cast basalt as an energy storage material
2. Complementing experiments with natural and cast basalt (density determination, dilatometry, evaluation of surface changes)
   - To further describe the behaviour of basalt at high temperatures
3. Experiments on packed and fluidized bed thermal storage
   - Comparison of the behaviour of packed and fluidized bed storage
   - Proposal of a multi-layered fluidized bed storage

Chapter 4

Behaviour of basalt at high temperatures for use in thermal energy storage

Natural and cast basalt are viable candidates for Carnot battery TES and therefore chosen to be investigated in this dissertation. This general assumption is based on the basalt's chemical composition, density, and approximate heat capacity. It should be the basis for further analysis, which will be outlined in this chapter.

4.1 Natural and cast basalt as storage material for thermal energy storage in Carnot batteries

Packed bed TES stands out as an uncomplicated, well-researched possibility with the benefit of a direct heat transfer, which results in lower losses and a smaller set-up of the complete Carnot battery system. As the previous chapter shows, basalt is one of the interesting storage materials for packed bed TES due to its suitable thermodynamic properties, like high density and heat capacity as well as its thermal stability over a wide temperature range. It further has good abrasion resistance, and a low tendency to corrosion [67]. As a natural rock found plenty in nature, it further poses the benefit that the impact on the environment due to acquisition is low.

The research on basalt as TES material has big gaps in the knowledge about the basalts performance at high temperatures and its temperature-dependant behaviour. On top of that, it also completely lacks analysis of realistically sized samples. For these reasons, basalt was chosen as the storage material to be investigated in this dissertation thesis.

However, not only natural basalt (Fig. 4.1a), but also cast basalt (Fig. 4.1b) is analysed in this thesis. Cast basalt, used as for example flue gas pipes, iron slurries, coal pipes or hoppers, has suitable thermal properties as well and wasn't yet considered for the use in TES.

(a) Natural basalt. (b) Cast basalt.

Figure 4.1: Pieces of natural and cast basalt [KR3]

The origin of the rocks used for the experiments in this thesis is Slapany u Chebu in the west of the Czech Republic. The company EUTIT s. r. o., located in Stará Voda (Cheb, Czech Republic), is the producer of the cast basalt product and kindly provided samples of both. The manufacturing process starts with melting the rock at 1280°C [68]. It is then cast into moulds and cylinders, which will then be put into kilns at 850°C for thermal treatment, forcing the basalt to recrystallize and change its properties. The temperature it can withstand now is 450°C. While the natural basalt (Figure 4.1a) already has a low tendency to corrosion and good abrasion resistance, the cast basalt (Figure 4.1b) is also inert, homogeneous, denser, non-porous, resistant to many chemicals and with higher abrasion resistance. The chemical composition, however, isn't changed a lot, as can be seen in Table 4.1 and Fig. 4.2.

Table 4.1: Chemical composition of natural basalt and the cast basalt product [KR3, 1].

Name	**Chemical formula**	**Natural Basalt**	**Basalt product**
Silicon dioxide	SiO_2	45.95 %	45.33 %
Aluminium oxide	Al_2O_3	12.74 %	12.44 %
Magnesium oxide	MgO	12.09 %	12.39 %
Calcium oxide	CaO	11.22 %	11.38 %
Iron(III) oxide	Fe_2O_3	11.36 %	11.37 %
Sodium oxide	Na_2O	2.98 %	2.96 %
Titanium dioxide	TiO_2	2.05 %	2.10 %
Potassium oxide	K_2O	1.03 %	0.94 %
Loss on ignition	-	0.58 %	1.09 %

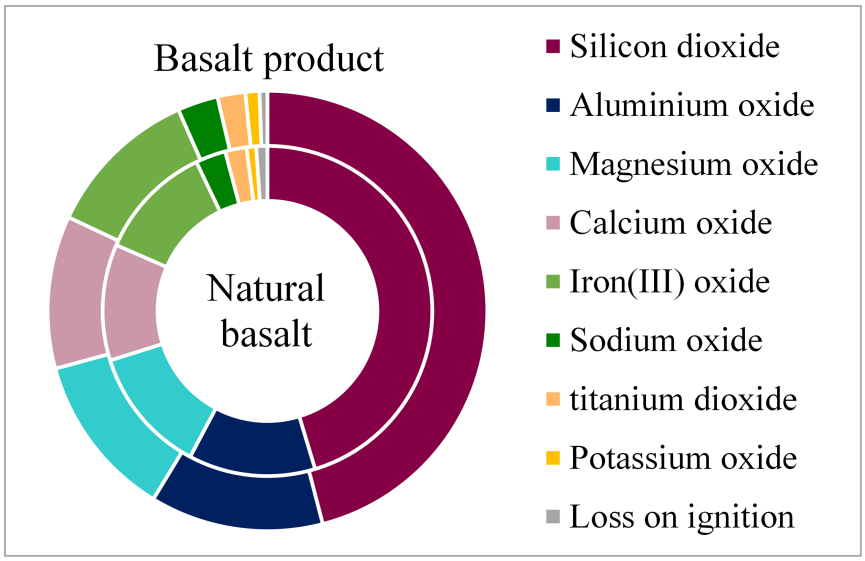

Figure 4.2: Graphic comparison of the chemical composition of natural basalt and the cast basalt product [KR3, 1]

4.2 Specific heat capacity and speed of reaching the full potential heat capacity

The specific heat capacity is probably the most important thermodynamic property concerning a rock's use as thermal energy storage material. Knowing how fast it can be utilised to the full extent and being aware of a materials charging and discharging speed allows to describe and predict a storage's behaviour and can help to optimise it.

4.2.1 Experimental investigation of the specific heat capacity

The specific heat capacity was determined experimentally. First, the experimental procedure will be explained, followed by the results and discussion section, as well as the validation of the results.

4.2.1.1 Experimental procedure and methodology

The specific heat capacity was determined with a calorimeter, as shown in Fig. 4.3 and Fig. 4.4. The method is based on that heat Q_r (4.1) is stored within a rock r with the mass m_r when it is heated to a certain temperature. The initial temperature of the rocks is room temperature (RT). They are heated to different temperatures denoted with $x°C$, where they have the heat capacity $c_{p,r,x°C}$. The heat stored in this way can be described as $\Delta Q_{r,(RT)to(x°C)}$ (4.2). The experimental procedure, as well as most results, were presented at the IRES conference 2021 and published in [KR3] and will not be repeatedly cited

individually.

$$Q_r = \Delta Q_{r,(RT)to(x°C)} \tag{4.1}$$

$$\Delta Q_{r,(RT)to(x°C)} = m_r \cdot c_{p,r,(x°C)} \cdot \Delta T_{r,(RT)to(x°C)} \tag{4.2}$$

During the heat capacity measurement, the rock is releasing heat to the water of the calorimeter (4.3).

$$\Delta Q_{r,(w)} = \Delta Q_w \tag{4.3}$$

Together with the temperature difference of the water (after measuring) to the room temperature, the total heat stored in the rock over the charging time can be determined (4.4).

$$\Delta Q_{r,(RT)to(x°C)} = \Delta Q_{r,(w)}) + \Delta Q_{r,(RT)} \tag{4.4}$$

The heat released into the water is

$$\Delta Q_w = m_w \cdot c_{p,w} \cdot (T_{w,ac} - T_{w,bc}) \tag{4.5}$$

with the mass m_w and the heat capacity $c_{p,w}$ of the water. The water temperature before cooling down the rock is $T_{w,bc}$, afterwards $T_{w,ac}$. The heat capacity of the water is approximated and assumed to be

$$c_{p,w} \approx 4182 \frac{J}{kgK} \tag{4.6}$$

for all temperatures. The remaining heat, stored due to the temperature difference of the water after the cooling ($T_{w,ac}$) to the room temperature $T_{(RT)]}$, is denoted in the following as $\Delta Q_{r,(RT)}$.

$$\Delta Q_{r,(RT)} = m_r \cdot c_{p,r,(w,ac)} \cdot (T_{w,ac} - T_{(RT)]}) \tag{4.7}$$

The heat capacity of the rock at $20°C$ is approximated according to Waples and Waples [2], which is sufficient as the variation of the basalt's heat capacity at the water's temperatures (about $15°C$ to maximum $30°C$), as well as the influence on the overall result, is minimal. The value is also used for the cast basalt product, primarily assuming it is similarly based on the nearly identical chemical composition of the cast and natural basalt. In reality, however, these values differ from each other, as can be said based on the results of this research.

$$\begin{aligned} c_{p,r,(w,ac)} &\rightarrow c_{p,r,(20°C)]} \\ c_{p,r,(20°C)]} &= 898 \frac{J}{kgK} \end{aligned} \tag{4.8}$$

The heat capacity $c_{p,r,(x°C)}$ of the rock, at the temperature $x°C$ is then calculated as

$$\begin{aligned} c_{p,r,(x°C)} &= \frac{Q_r}{m_r \cdot \Delta T_{r,(x°C)to(RT)}} \\ &= \frac{\Delta Q_w + \Delta Q_{r,(RT)}}{m_r \cdot \Delta T_{r,(x°C)to(RT)}} \\ &= \frac{m_w \cdot c_{p,w} \cdot (T_{w,ac} - T_{w,bc}) + m_r \cdot c_{p,r,(w,ac)} \cdot (T_{w,ac} - T_{(RT)})}{(m_r \cdot (T_{r,(x°C)} - T_{(RT)]})} \end{aligned} \tag{4.9}$$

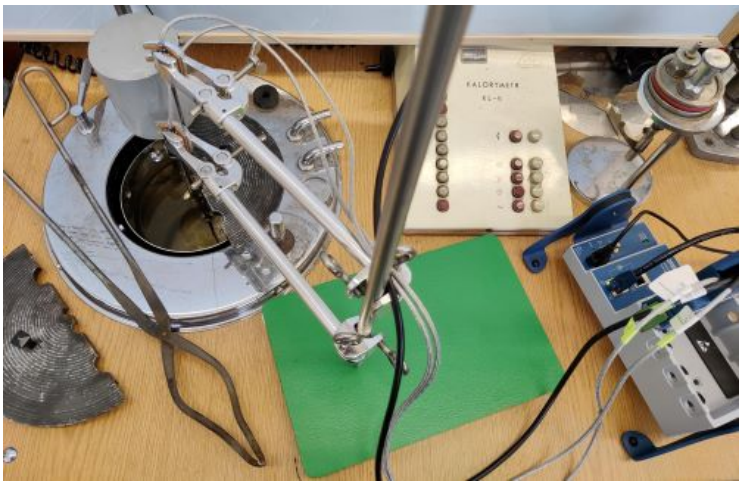

Figure 4.3: Calorimeter for determining the heat capacity of the rock patterns [KR3].

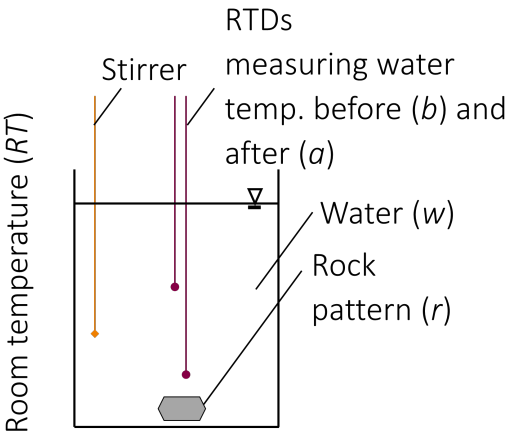

Figure 4.4: Schematic display of the calorimeter [KR3].

To determine the speed of reaching the full potential heat capacity, ten rock patterns (Fig. 4.5b) are put into the furnace at $300°C$ to $750°C$ (Fig. 4.5a). With an interval of three minutes, a pattern is removed and put into the calorimeter using a metal claw. The heat capacity is then calculated based on the water's temperature rise. An insulated steel bucket filled with 3.5 to 4 litres of water, insulated with a lid on top to prevent temperature exchange with the environment, is the basis of the calorimeter Fig. 4.4. A stirrer, keeping the water in motion, prevents temperature stratification within the tank and speeds up the cooling of the rocks. Two RTD sensors measure the water temperature and are further used to detect possible temperature stratification. The room temperature is measured with a third RTD sensor. All data is acquired with a National Instruments Module (9226), connected to a National Instruments Compact DAQ Chassis (cDAQ 9185) and evaluated in LabVIEW.

For cooling, a second low-temperature furnace is set to $100°C$. After 30 minutes, the

(a) *Furnace.*

(b) Layout of rock patterns.

Figure 4.5: Furnace for heating up the rock patterns [KR3].

rocks are transferred from the high-temperature furnace to the 100°C environment. The rocks used in this set of experiments have holes drilled to the centre in which a thermocouple is inserted to determine the real rock temperature. The rock's real temperature is necessary for calculating the heat capacity, as the oven temperature, in this case, doesn't allow any assumption of the temperature. For the heating process, this method isn't possible as the insulation of the furnace doesn't allow an application of a thermocouple. Therefore, the simplified static change of heat capacity is used for the charging process, while the slightly more accurate method with the rock's real temperature is used for the change of heat capacity during cooling.

4.2.1.2 Results and discussion - Heating

The natural basalt's full potential heat capacity is reached after 24 minutes at 300°C and 400°C, after 12 minutes at 500°C, 600°C and 700°C, and after 15 minutes at 750°C [KR3]. The trend is that the full potential heat capacity is reached faster with higher temperatures, as is also visualised in Fig. 4.6. The speed of reaching the full potential heat capacity is increasing from 0.50 (J/(kg*K))/s at 300°C until 1.35 (J/(kg*K))/s at 600°C to 750°C (Fig. 4.9).

Between 500°C and 700°C and above 750°C, the full potential heat capacity is reached faster with the cast basalt product than with the natural basalt, i.e. the speed of reaching the full potential heat capacity is higher. In particular, the speed is 0.66 (J/(kg*K))/s at 300°C and 1.82 (J/(kg*K))/s at 750°C (Fig. 4.9), After only 21 minutes at 300°C, 18 minutes at 400°C and 500°C, 15 minutes at 600°C, 12 minutes at 700°C and 9 minutes at 750°C, the cast basalt product reaches its full potential heat capacity (Fig. 4.7). There wasn't observed any obvious difference for the cast basalt material at temperatures above 450°C, which is its limit temperature, guaranteed by EUTIT.

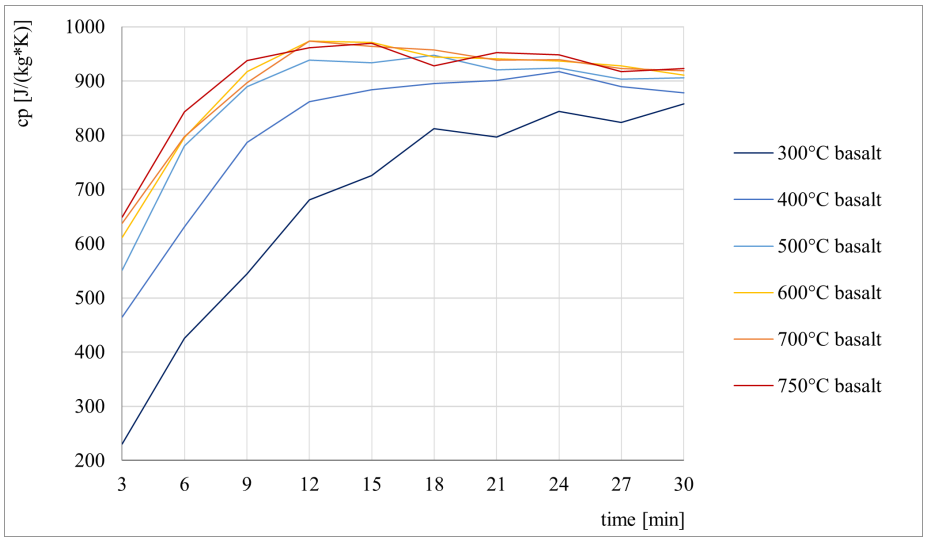

Figure 4.6: Static change of the natural basalts heat capacity (samples 46g – 73g) [KR3].

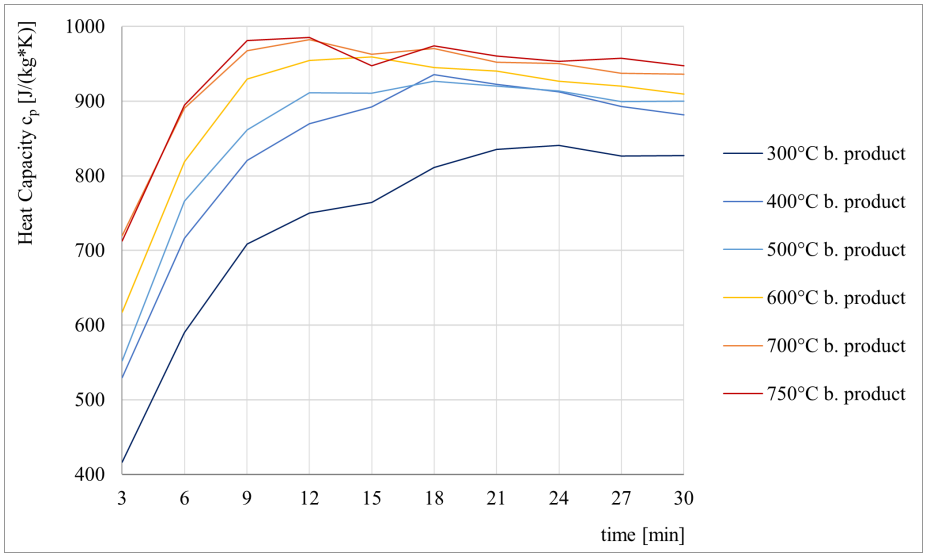

Figure 4.7: Static change of the basalt products heat capacity (samples 43g – 64g) [KR3].

The used samples have a similar weight. The natural basalt samples weigh between 46g and 73g, while the samples of the cast basalt weigh between 43g and 64g. To show the importance of this and to display the dependency on the size, a second row of experiments was done with natural basalt weighing between 18g and 38g (Fig. 4.8). Slightly higher heat capacities are reached faster than with the heavier samples (Fig. 4.9).

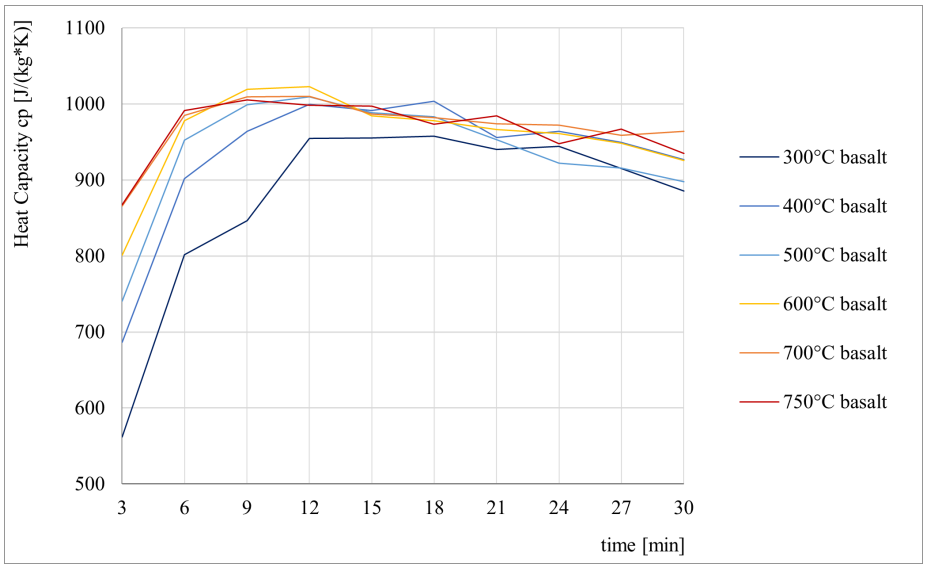

Figure 4.8: Static change of the naturals basalt heat capacity (samples 18g – 38g) [KR3].

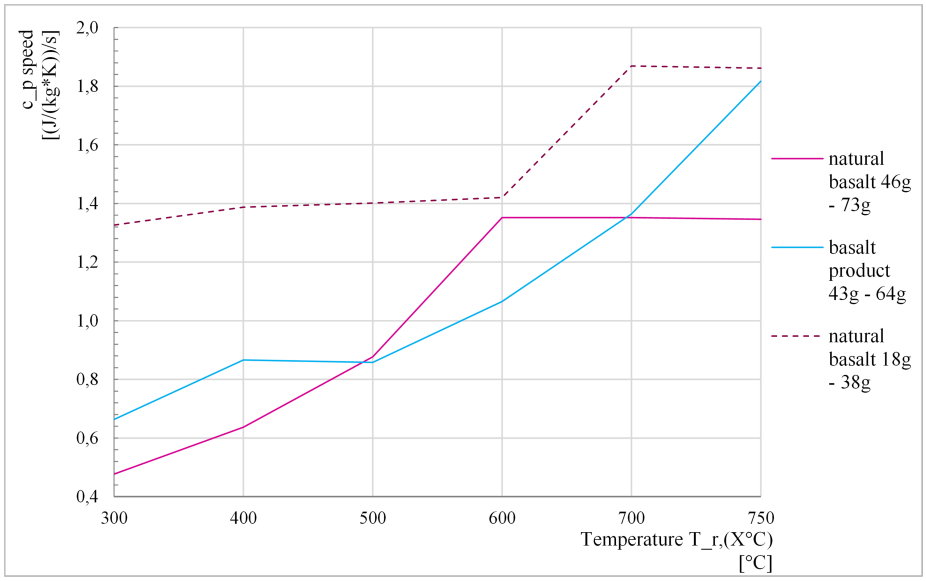

Figure 4.9: Speed of reaching the full potential heat capacity [KR3].

The heat capacity is quite similar for all temperatures and, for both materials, it increases to a maximum value before decreasing again. Comparing the full potential heat capacity after 30 minutes to the maximum value, the basalt product deviates up to 4.1 % and the cast basalt up to 4.0 %. The final full potential heat capacity for temperatures of $300°C$ to $750°C$ after 30 minutes of heating varies up to 13 % for the basalt product and up to 7 % for the natural basalt.

As water has a several times higher heat capacity than the rocks, which is increasing exponentially at temperatures greater $200°C$ [69], a partial explanation for this might be the

evaporation of water from the rock's pores during the first minutes of the heating process. A possibility to prevent this would be drying the rocks at a lower temperature over a longer period. However, the influence of the possibly evaporating water isn't expected to be high when comparing the individual measurements and because similar results of the individual rock pieces, which can be seen after 3 to 30, 33 to 60 and 63 to 90 minutes of heating (Fig. 4.10). Furthermore, drying the rocks might already influence their heat capacity, as also stated by Knobloch et al. [53]. The more likely reason for the effect, visible in the results at hand, is the individual chemical composition of the rocks. As non-homogeneous material, the natural basalt also shows slightly greater irregularities in the heat capacity after reaching its maximum value than the basalt product, which is due to the melting and casting process, a more homogeneous product. The smaller a sample, the greater the influence of the rock's composition, backing the just mentioned thesis (compare Fig. 4.6 and Fig. 4.8).

In Fig. 4.10, another interesting effect can be perceived. Already during the third time heating the rocks (results are shown at 60 minutes plus), the total heat capacity reached, decreases, and the difference between the various samples gets smaller (every 3 minutes measurement point represents a different sample, see the experimental setup in chapter 4.2.1.1). This degradation of the materials thermal stability, the decrease to a more equal, minimum heat capacity, was also observed by the thermal storage team at the Danish Technical University in their lab-scale storage test facility *Droplet* [53], as well as by Becattini et al. [3] in their laboratory experiments, cycling different material with a furnace. Both are using differential scanning calorimetry (DSC) for measuring the heat capacity, Knobloch et al. [53] at all with pulverised samples and Beccatini et al. [3] with samples of 5 mm length and a mass of about 60 mg. Beccatini et al. found a decrease in the specific heat capacity at $550°C$ of almost 40 % after 40 cycles. The DTU observed a decrease of specific heat capacity of their storage material diabase already from the second run, with a final decrease from the original 970 J/(kg*K) in the first run to 860 J/(kg*K) after 249 cycles at up to $600°C$ in the demonstrator (an average decrease of 12.8 % between $50°C$ and $600°C$ [53]. A heat capacity of 1120 J/(kg*K) was given in their supplier's datasheets. They further explain the difference between their first run and the supplier's data with the 6 hours of drying the rocks at $90°C$. This effect was not encountered in this dissertation's work, as drying didn't take place. The experiments presented in this thesis, using a totally different type of calorimetric measurement and a hugely different type of samples (rock pieces of 18 g to 73 g with several centimetres in diameter), show similar behaviour. That the heat capacity already decreases with the first cycles, as for the team at DTU [53] can also be confirmed. The reason, according to Beccatini et al. [3] is, that felsic rock, i. e. also basalt, is high in chlorite, which has a dehydration temperature greater $400°C$ [70], which is below the maximum cycling temperature. However, an important difference is that the decrease in heat capacity for the basalt is lower than for other felsic rock, like diabase. The maximum decrease measured after two cycles about 4 % for both materials. This might be due to a lower amount of iron in the basalt rocks.

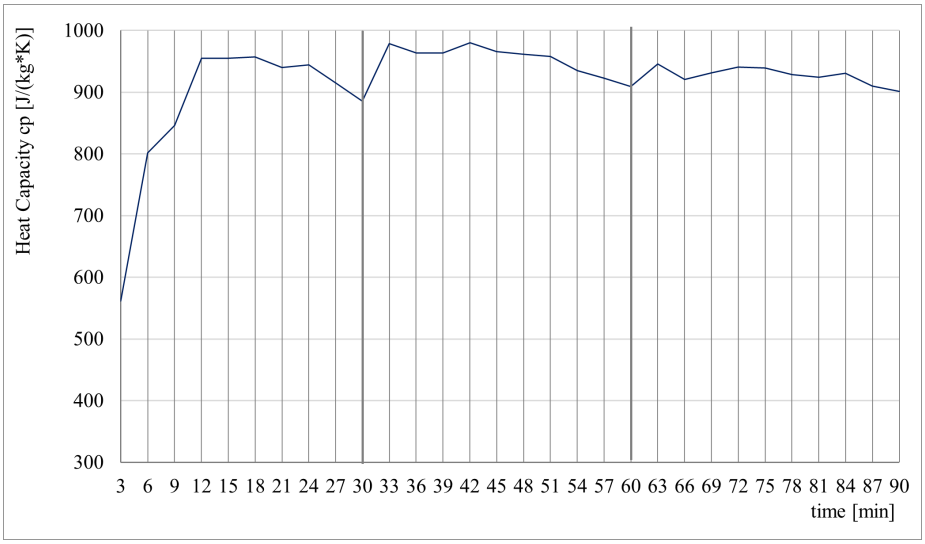

Figure 4.10: Static change of the natural basalts heat capacity over a period of 90 minute at 300°C (samples 18g – 38g) [KR3].

4.2.1.3 Results and discussion - Cooling

To naturally cool the rocks to $100°C$ takes 21 to 30 minutes for the natural basalt (Fig. 4.11) and 21 to 27 minutes for the cast basalt product (Fig. 4.13) [KR3]. The heat capacity of the natural basalt falls to the rock's heat capacity at $100°C$ within 12 minutes (Fig. 4.12) and within only 3 minutes for the cast basalt (Fig. 4.14). The fast cooling of the rocks indicates an effective discharge of the stored thermal energy. Another proof that the rock's specific chemical composition and size have a great influence on the heat capacity, as described in 4.2.1.2, is that the heat capacity is again unstable after reaching its $100°C$ value (see Fig. 4.11 to Fig. 4.14). The slight fluctuation of the temperature, after the patterns cooled to the $100°C$ environment, is caused by the used furnace, an older model of dryer, where the temperature cannot be set completely accurate. The influence on the results is very small, and therefore the inaccuracy is acceptable.

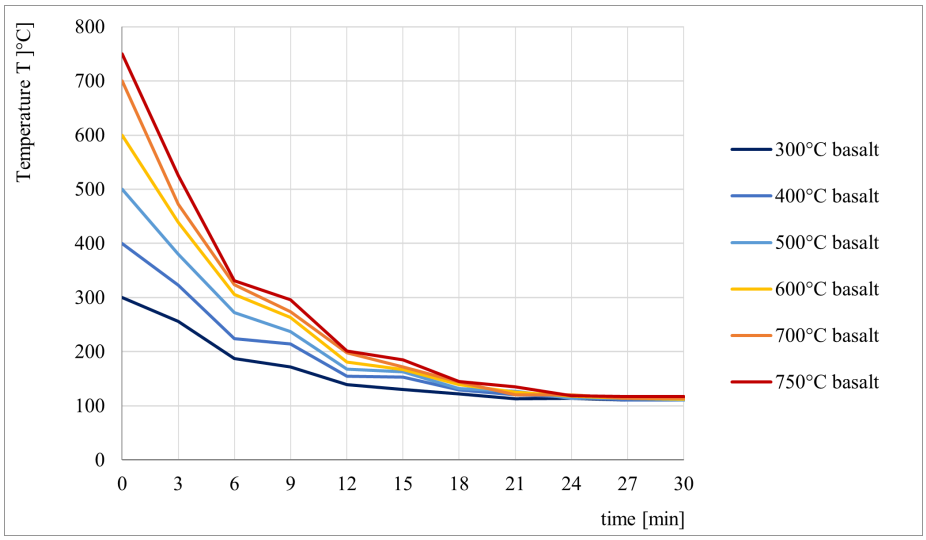

Figure 4.11: Natural basalt temperature during cooling (samples 72g – 103g) [KR3].

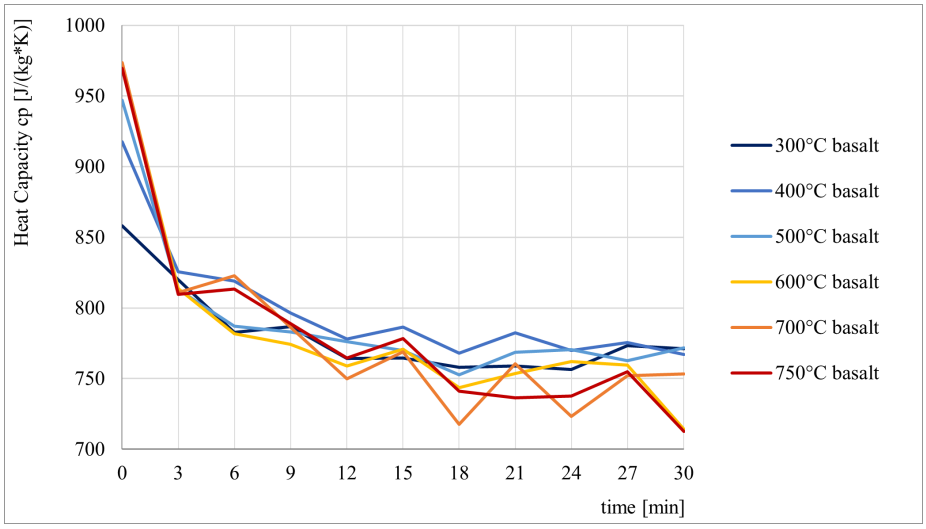

Figure 4.12: Natural basalt heat capacity during cooling (samples 72g – 103g) [KR3].

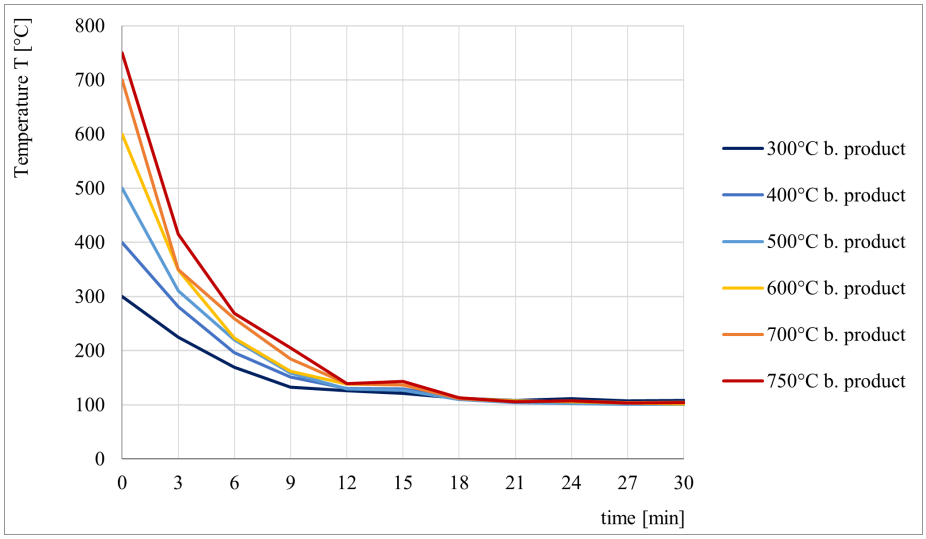

Figure 4.13: Basalt product temperature during cooling (samples 28g – 44g) [KR3].

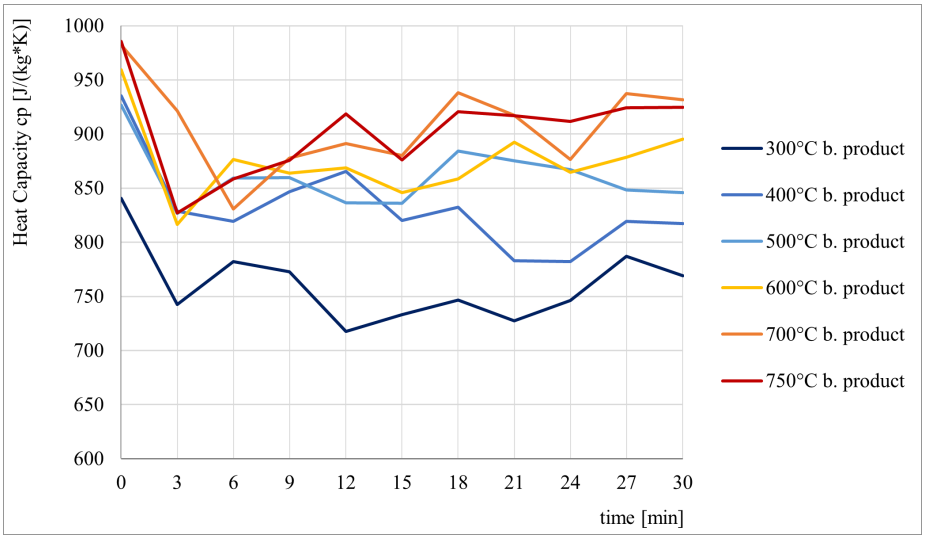

Figure 4.14: Basalt product heat capacity during cooling (samples 28g – 44g) [KR3].

4.2.1.4 Validation of the experiments

In Fig. 4.15, the maximally reached heat capacity is compared with other experimental and theoretical research [KR3]. Similar heat capacities were measured with also comparable effects, like a dropping heat capacity at higher temperatures (see Martin et al. [4] and Nahhas et al. [6]). The experimental method can, therefore, be seen as validated. It should be mentioned that Martin et al. don't explain the different heat capacity series they measured. They only acknowledge it and continue to use the average of the three results for further work. However, with the knowledge from this work, it can be seen as another strong argument for the great influence of the chemical composition of the individual rocks.

The theoretical estimate of the rocks heat capacity based on Waples & Waples [2] and Becattini et al. [3] are far off from the experimental results of this and other work, as can also be seen in Fig. 4.15 [1]. Therefore, an accurate model, not only depicting the heat capacity over the temperature but also over time, a model of the speed of reaching the full potential heat capacity, was prepared and will be explained in chapter 4.2.2.

[1] From this work, the heat capacity values at the time $t = 24min$ for up to $400°C$ and at $t = 12min$ for temperatures of $450°C$ and above, were used.

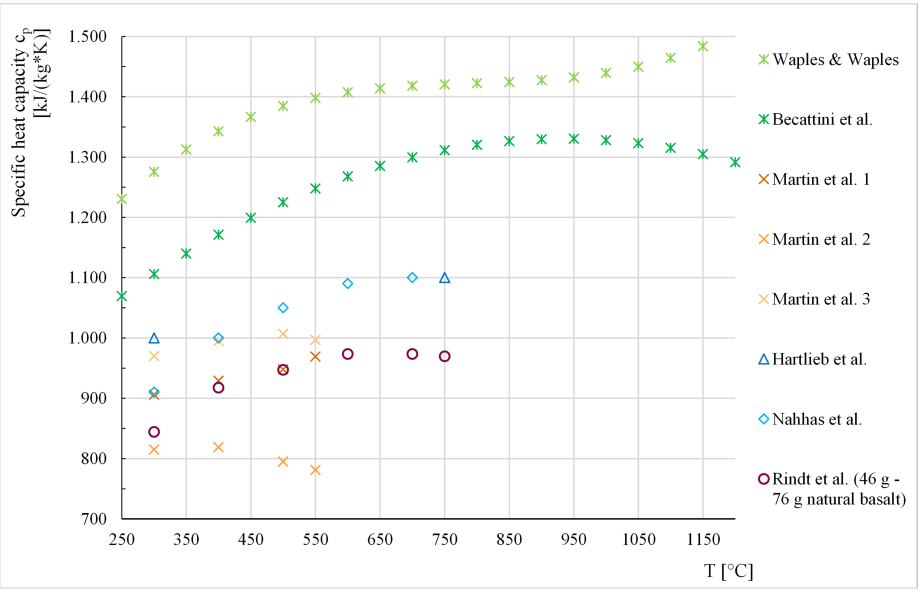

Figure 4.15: Heat capacity of basalt rock – comparison with other experimental research and theoretical calculations [KR3, 2–6].

4.2.2 Mathematical model

In this chapter, a model of the specific heat capacity of natural and cast basalt is suggested. However, a physical correlation exists only between the temperature and the heat capacity and not to the time, which visualises the charging behaviour. Therefore, the model is a 4^{th}-grade polynomial fitted to the experimental data, solved by the least-squares method, and not a partial differential equation. The mathematical model was presented at the ENERSTOCK conference 2021, and an article is in review [KR5]. Therefore much content is overlapping with the article, which won't be repeatedly cited individually.

4.2.2.1 Method of least squares

The method of least squares is described using Blobel & Lohrmanns "Statistische und numerische Methoden der Datenanalyse" [71]. The specific heat capacity data of the experiments is represented by arbitrary variables y_i, $i = 1, 2, ...n$, where n is the number of measurements. Parameters, defined as α_j, $j = 1, 2, ...p$, and conditions, equations of the type (4.10), are needed for the model.

$$f(\alpha_1, \alpha_2, ...\alpha_p, y_1, y_2, ...y_n) = 0 \tag{4.10}$$

The conditions model is then used to find the correctors Δy for the measurement values y_i, which then fulfil the conditions exactly. The correctors are the residues, or in other words, the differences between the data and the model. The method of least squares demands that the sum of squares of the residues is minimised as expressed as (4.11) for the

simplest case of n-times measured values y_i of the variables y and as (4.12) for a function $f(x_i, a)$ which is linear dependant on p parameters a_i with the residues $r_i = y_i - f(x_i, a)$.

$$F = \sum_{i=1}^{n} \Delta y_i^2 = \sum_{n=1}^{n} \Delta (y - y_i)^2 = Minimum \tag{4.11}$$

$$F(\alpha_i) = \sum_{i=1}^{n} r_i^2 = \sum_{i=1}^{n} (y_i - \alpha_1 f_1(x_i) - \alpha_2 f_2(x_i) - \alpha_p f_p(x_i))^2 \tag{4.12}$$

Writing this for a 4^{th}-grade polynomial $P(t_i, T_j)$ with two variables t_i and T_j which have $i = 1, 2, ...n$ and $j = 1, 2, ...m$ possible values (4.13), the equation $F(\alpha_{ij})$ needs to be minimized according to (4.14).

$$\begin{aligned} P[t_i, T_j] = {} & (\alpha_{00} \cdot 1) + (\alpha_{10} \cdot t + \alpha_{01} \cdot T + \alpha_{11} \cdot t \cdot T) \\ & + (\alpha_{20} \cdot t^2 + \alpha_{02} \cdot T^2 + \alpha_{21} \cdot t^2 \cdot T + \alpha_{12} \cdot t \cdot T^2 \\ & + \alpha_{22} \cdot t^2 \cdot T^2) + (\alpha_{30} \cdot t^3 + \alpha_{03} \cdot T^3 + \alpha_{31} \cdot t^3 \cdot T \\ & + \alpha_{13} \cdot t \cdot T^3 + \alpha_{32} \cdot t^3 \cdot T^2 + \alpha_{23} \cdot t^2 \cdot T^3 \\ & + \alpha_{33} \cdot t^3 \cdot T^3) + (\alpha_{40} \cdot t^4 + \alpha_{04} \cdot T^4 + \alpha_{41} \cdot t^4 \cdot T \\ & + \alpha_{14} \cdot t \cdot T^4 + \alpha_{42} \cdot t^4 \cdot T^2 + \alpha_{24} \cdot t^2 \cdot T^4 + \\ & \alpha_{43} \cdot t^4 \cdot T^3 + \alpha_{34} \cdot t^3 \cdot T^4 + \alpha_{44} \cdot t^4 \cdot T^4) \end{aligned} \tag{4.13}$$

$$F(\alpha_{ij}) = \sum_{i=1}^{n} \sum_{j=1}^{m} (y_{ij} - P(t_i, T_j))^2 \tag{4.14}$$

As a constraint for the minimization, all partial derivatives to the parameters α_{ij} need to disappear (4.15).

$$\min_{\alpha} F(\alpha_{ij}) \quad \Rightarrow \quad \frac{F(\alpha_{ij}}{\partial(\alpha_{00})} = 0 \quad ... \quad \frac{F(\alpha_{ij}}{\partial(\alpha_{44})} = 0 \tag{4.15}$$

For the 4^{th}-grade polynomial, the derivation is solved as in (4.16), with $f_p(t_i, T_j)$ describing the parts of the polynomial attached to the corresponding parameter α_p, i. e. the linear combinations of time t_i and temperature T_j: $f_1(t_i, T_j) = 1$, $f_2(t_i, T_j) = t$, $f_3(t_i, T_j) = T$, ..., $f_p(t_i, T_j) = t^4 T^4$.

$$\begin{aligned} \frac{F(\alpha_{ij})}{\partial(\alpha_{00})} = {} & 2 \sum_{i=1}^{n} \sum_{j=1}^{m} f_1(t_i, T_j) \cdot (\alpha_{00} f_1(t_i, T_j) + \\ & + \alpha_{10} f_2(t_i, T_j) + ... + \alpha_{44} f_p(t_i, T_j) - y_{ij}) = 0 \end{aligned}$$

$$...$$

$$\begin{aligned} \frac{F(\alpha_{ij})}{\partial(\alpha_{44})} = {} & 2 \sum_{i=1}^{n} \sum_{j=1}^{m} f_p(t_i, T_j) \cdot (\alpha_{00} f_1(t_i, T_j) + \\ & + \alpha_{10} f_2(t_i, T_j) + ... + \alpha_{44} f_p(t_i, T_j) - y_{ij}) = 0 \end{aligned} \tag{4.16}$$

The constraint (4.16) can also be written in the form of a normal equation (4.17).

$$\begin{aligned}\alpha_{00}\sum_{i=1}^{n}\sum_{j=1}^{m} f_1(t_i,T_j)^2 + ... + \alpha_{44}\sum_{i=1}^{n}\sum_{j=1}^{m} f_1(t_i,T_j)f_p(t_i,T_j) \\ = \sum_{i=1}^{n}\sum_{j=1}^{m} y_{ij}f_1(t_i,T_j)\end{aligned}$$

$$... \tag{4.17}$$

$$\begin{aligned}\alpha_{00}\sum_{i=1}^{n}\sum_{j=1}^{m} f_p(t_i,T_j)f_(t_i,T_j)1 + ... + \alpha_{44}\sum_{i=1}^{n}\sum_{j=1}^{m} f_p(t_i,T_j)^2 \\ = \sum_{i=1}^{n}\sum_{j=1}^{m} y_{ij}f_p(t_i,T_j)\end{aligned}$$

According to the least-squares method, the p resulting estimates α_{00} to α_{44} are the solution of these normal equations.

4.2.2.2 Numerical solution

The system of equations was solved numerically, finding the 25 parameters α_{ij}. The solution of each least-squares equation needs to be converted into matrix notation (4.18). A vector y with $n \cdot m$ rows (4.19) represents the data and a matrix A (4.20) with $(n \cdot m)$ rows and p columns, represents the polynomial $f_{ij}(t_i, T_j)$. p are the number of parameters α_p of the matrix A, which are written as a vector with p rows (4.21). The residues are then $r = y - A\alpha$.

$$\begin{aligned}F = r^T r &= (y - A\alpha)^T(y - A\alpha) \\ &= y^T y - 2a^T A^T y + a^T A^T A a = Minimum\end{aligned} \tag{4.18}$$

$$y = \begin{pmatrix} y_{11} \\ y_{12} \\ . \\ . \\ . \\ y_{nm} \end{pmatrix} \tag{4.19}$$

$$A = \begin{pmatrix} f_{11}(t_i,T_j) & f_{21}(t_i,T_j) & ... & f_{p1}(t_i,T_j) \\ f_{12}(t_i,T_j) & f_{22}(t_i,T_j) & ... & f_{p2}(t_i,T_j) \\ . & & & \\ . & & & \\ . & & & \\ f_{1(nm)}(t_i,T_j) & f_{1(nm)}(t_i,T_j) & ... & f_{p(nm)}(t_i,T_j) \end{pmatrix} \tag{4.20}$$

$$a = \begin{pmatrix} \alpha_{00} \\ \alpha_{10} \\ . \\ . \\ . \\ \alpha_{44} \end{pmatrix} \tag{4.21}$$

The condition for the minimum of (4.18) is (4.22).

$$-2A^T y + 2A^T A\hat{a} = 0 \tag{4.22}$$

Writing the condition for the minimum (4.22) in the matrix form of the normal equation (4.23) with $A^T A$ being a symmetric p x p matrix and $A^T y$ a p-vector, the equations (4.23, 4.24) can be solved with standard methods of the matrix algebra.

$$A^T A\alpha = A^T y \tag{4.23}$$

$$\hat{a} = (A^T A)^{-}1A^T y \tag{4.24}$$

4.2.2.3 Model of specific heat capacity – 4th-grade polynomial

The solution of the 4th-grade polynomial $P(t_i, T_j)$, models the specific heat capacity $c_p = [J/(kgK)]$ over time $t = [min]$ and temperature $T = [°C]$ and is applicable from 300°C to 750°C. A use beyond these boundaries isn't possible because 4th-grade polynomials naturally diverge strongly outside the range of the underlying data. However, a use of the basalt at higher temperatures would also not be recommended as it would result in structural changes (the recrystallisation temperature of basalt is 850°C). The charging model of natural basalt (46 g to 76 g) is shown in Fig. 4.16 and the model of cast basalt (43 g to 64 g) in Fig. 4.17. The experimental data, marked with *, is represented well by the models, which can, therefore, be used for predicting the natural and cast basalts heat capacity at any temperature between 300°C to 750°C as well as how it changes during the heating process.

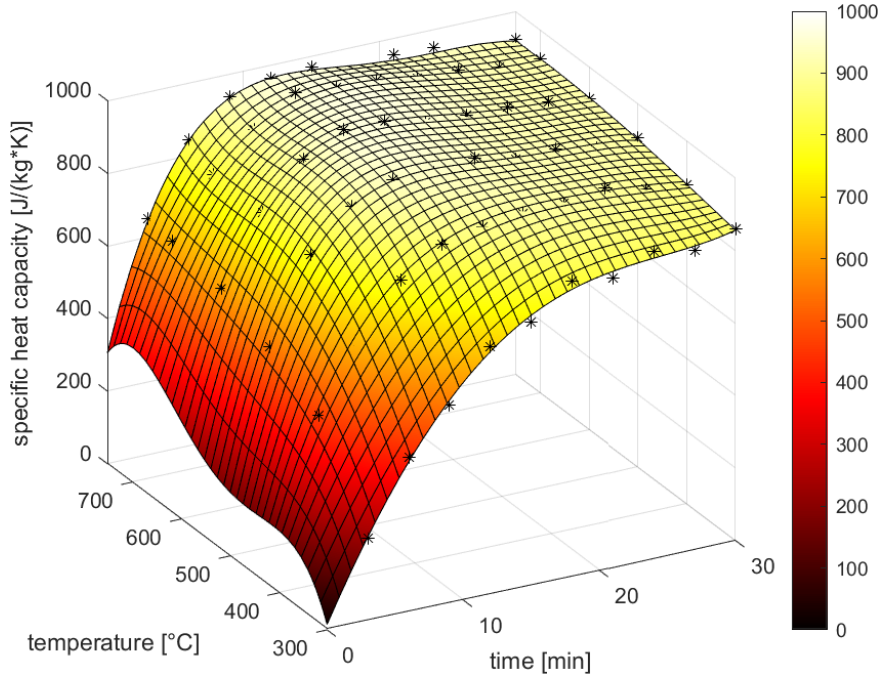

Figure 4.16: Model of the specific heat capacity over time and temperature during charging (46 g to 76 g natural basalt) [KR5].

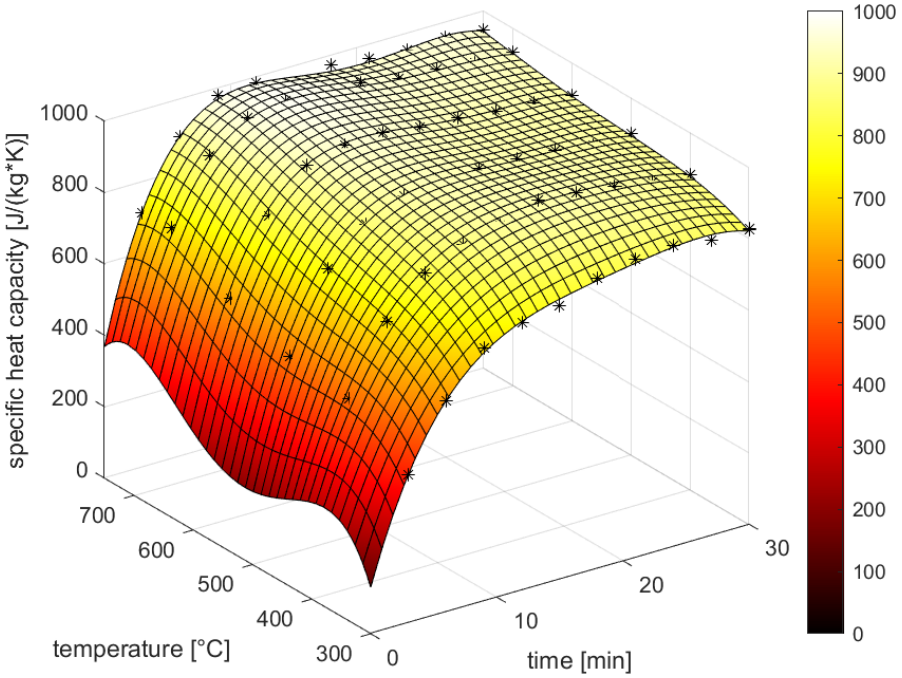

Figure 4.17: Model of the specific heat capacity over time and temperature during charging (43 g to 64 g basalt product) [KR5].

The coefficients α_{ij} of the solved 4th-grade polynomial $P(t_i, T_j)$ for the hating up case, are listed in Table 4.2.

Table 4.2: Coeficcients α_{ij} for the 4th-grade polynomial $P(t_i, T_j)$ [KR5].

	basalt product	**natural basalt**
α_{00}	-11110,1790740903000	-8835,2623655630300
α_{10}	2802,0389752105900	2947,3925652639500
α_{01}	93,9328995631543	73,6742306933777
α_{11}	-22,8153440230081	-26,2892407875051
α_{20}	-285,0725291787270	-311,5463342532230
α_{02}	-0,2822967943355	-0,2219754189974
α_{21}	2,3329702618730	2,8657829854241
α_{12}	0,0694101180089	0,0859830363000
α_{22}	-0,0070422926205	-0,0094499540781
α_{30}	11,3792171553896	12,4257655842344
α_{03}	0,0003649313055	0,0002907624802
α_{31}	-0,0930249968719	-0,1155545786037
α_{13}	-0,0000899335913	-0,0001182743435
α_{32}	0,0002794667455	0,0003822676869
α_{23}	0,0000090752226	0,0000130730416
α_{33}	-0,0000003594938	-0,0000005306276
α_{40}	-0,1529418499725	-0,1652349311711
α_{04}	-0,0000001710927	-0,0000001388074
α_{41}	0,0012472865766	0,0015498370583
α_{14}	0,0000000422175	0,0000000583001
α_{42}	-0,0000037374088	-0,0000051501827
α_{24}	-0,0000000042510	-0,0000000064752
α_{43}	0,0000000048073	0,0000000071801
α_{34}	0,0000000001685	0,0000000002637
α_{44}	-0,0000000000023	-0,0000000000036

The model of the specific heat capacity during discharging is visualised for basalt pieces of 46 g to 76 g in Fig. 4.18 and for the basalt product with 43 g to 64 g in Fig. 4.19. The natural inhomogeneity of the rocks causes a variation in the results, as described in chapter 4.2.1.1. These fluctuations in heat capacity result in a less accurate, more representative model of heat capacity change during cooling down.

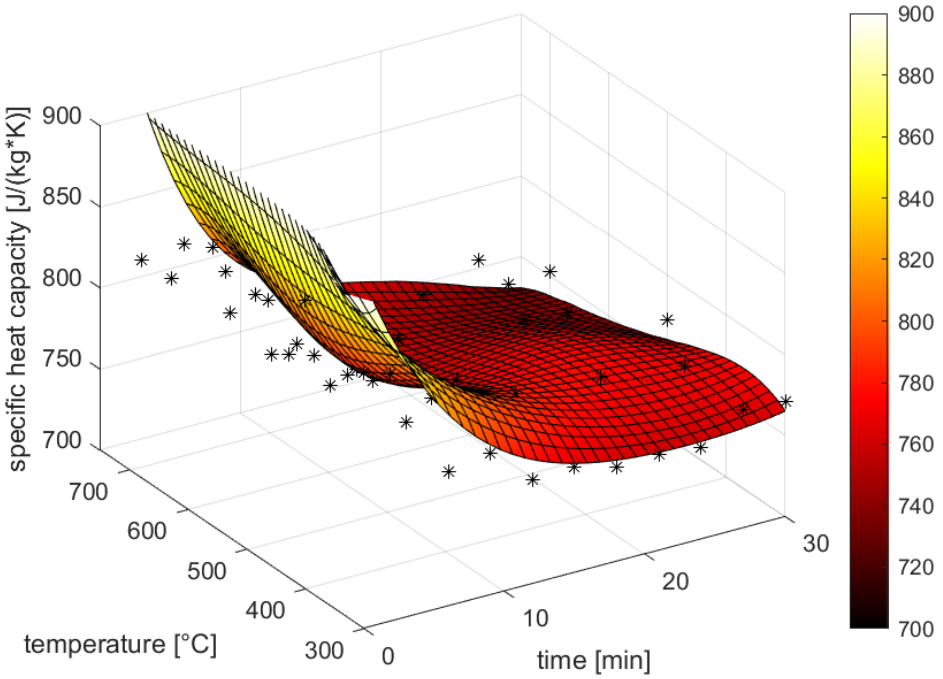

Figure 4.18: Model of the specific heat capacity over time and temperature during discharging (46 g to 76 g natural basalt) [KR5].

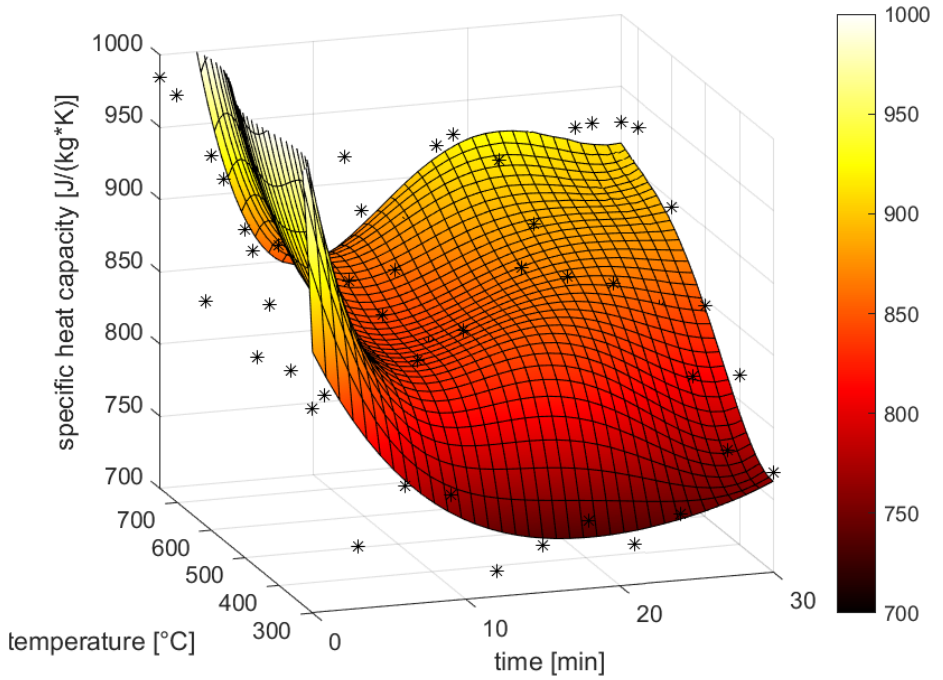

Figure 4.19: Model of the specific heat capacity over time and temperature during discharging (43 g to 64 g basalt product) [KR5].

4.2.2.4 Validation of the mathematical model

To show that the mathematical model is not only fitting the experimental data but that it is also more accurate than other available models, Fig. 4.20 (an extension of Fig. 4.15) shows a comparison of the maximum heat capacity per temperature.

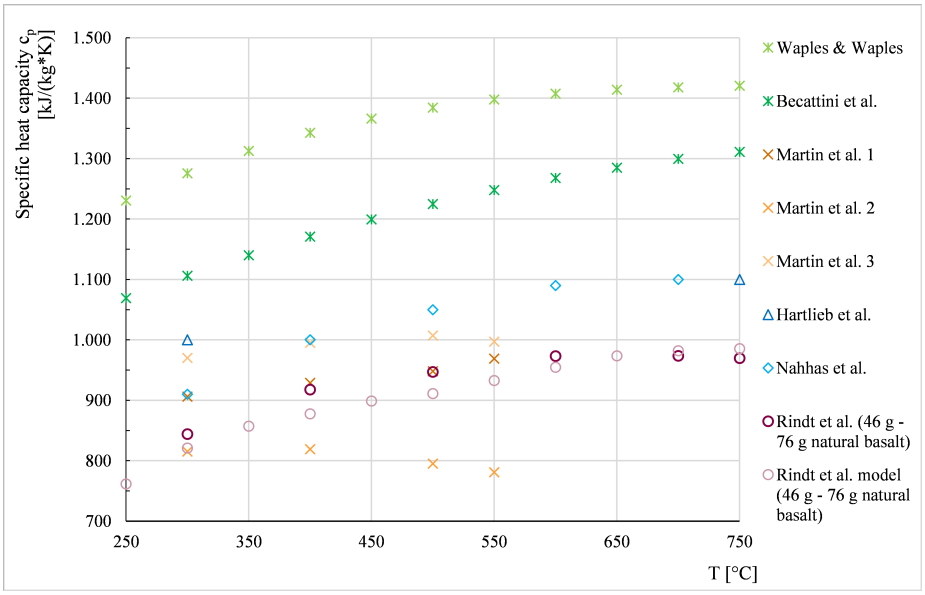

Figure 4.20: Heat capacity of basalt rock – comparison with other experimental research and theoretical calculations (for this work with 46 g to 76 g natural basalt) [KR3,KR5,2–6].

4.3 Surface changes

Weight and surface changes of the natural and cast basalt due to the heating process were observed. Parts of the rock's surface changed from white red for both materials, starting with the first heating to 750°C (Fig. 4.21 natural basalt, Fig. 4.22 basalt product) [KR3]. This change is most likely some light corrosion, which is likely to be the cause of the observed weight loss of the material. The natural basalt's weight was reduced by 1.5 % in the first heating cycle, and the basalt product's weight by 0.06 %. The red color is getting more intensive with an increasing number of cycles, indicating that the tendency to corrosion might not be as low as expected. The corrosion could have negative impact on a storage life-time.

Figure 4.21: Surface changes of natural basalt (FLTR: before, after one, and after many heating cycles) [KR3].

Figure 4.22: Surface changes of the basalt product (FLTR: before, after one, and after many heating cycles [KR3].

4.4 Density

The density is an important parameter for selecting suitable rocks for thermal storage, influencing mainly the size and, therefore, the necessary containment material and insulation. Therefore, a density analysis was performed in cooperation with the Faculty of Civil Engineering [72], and the results will be shown in this chapter. The density measurement was presented at the STČ conference 2021 [KR4].

4.4.1 Experimental procedure and methodology

The density was determined once before any heating process and then again after one hour in the furnace at $750°C$. For determining the density, a helium pycnometer from the company Thermo Scientific as can be seen in Fig. 4.23, was used and the samples were pulverised.

Figure 4.23: Helium pycnometer [7].

4.4.2 Results and discussion

The results for the density measurement can be seen in Fig. 4.24. The natural basalts density is slightly higher than the cast basalt products density. Both have a density close to 3000 kg/m^3. Due to the heating process of one hour at 750°C, the natural basalt gets denser by 1.41 % while the basalt product gets denser by only 0.16 %. The change in density for the natural basalt is nine times higher than for the basalt product.

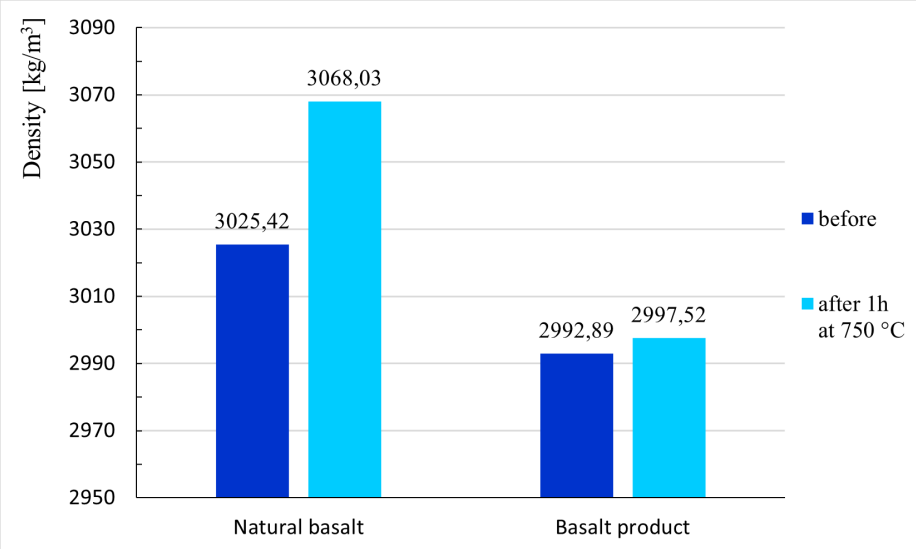

Figure 4.24: Density of natural and cast basalt before (at room temperature) and at 750 °C.

The change in density of the natural basalt resembles the change in the density of diabase after heating to 600°C (1.3 %), measured by Knobloch et al. [53].

4.5 Volumetric changes

The thermal expansion of storage material is likely to influence storage performance due to abrasion (possibility of problems due to tiny particles being carried away by the working fluid), cracking (possible change of thermal behaviour) or, to a certain degree, movement and restacking of the rocks (important for storage design). The latter was already observed in a lab-scale pilot [53]. The dilatometric measurement was presented at the STČ conference 2021 [KR4], and by the colleagues from the Faculty of Civil Engineering [72] at the THERMOPHYSICS conference 2021. An in-depth article is in print [KR6].

4.5.1 Experimental procedure and methodology

During the heating process, the linear volumetric changes were evaluated with a dilatometer from the company NETZSCH (DIL 402SE, Fig. 4.25). The heating rate was 10 K/min and with the maximum temperature set to 850°C to ensure that the sample reaches 750°C.

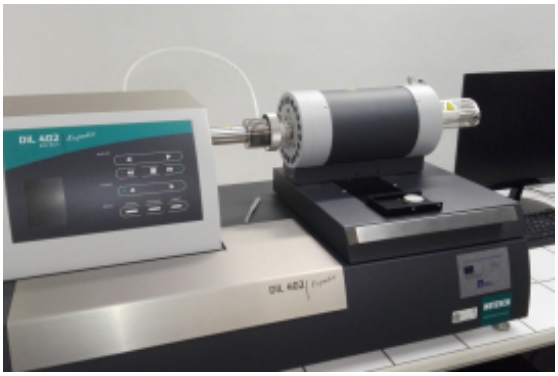

Figure 4.25: Dilatometer [8].

4.5.2 Results and discussion

The length of the raw basalt changes nearly proportional to its temperature rise (Fig. 4.26). During the first 20 min, heating is quite slow, reaching only 100°C in that period, despite the more than double as fast heating rate. The gradient of the heating curve (equaling approximately the curve of the length change) rises from 0.1 to 11.5 during the first 34 minutes (up to about 230°C) and then stays relatively constant for the rest of the heating. The maximum dilatation is at the highest temperature and amounts to 0.789 %. After 60 minutes, a step can be seen in the graph. This was most likely due to some dilatometer's mistake, as there is also a step in the applied force (black, horizontal, line). Therefore, the line should be moved transversally down according to the difference at the step. The basalt product's behaviour is quite similar, also about proportional with the temperature rise (Fig. 4.27), reaching a little higher maximum length change of 0.801 %. However, between 300°C and 750°C, the natural basalt's percental elongating is slightly higher than for the basalt product, rising faster than the temperature, with a maximum difference of

0.045 per cent points after around 67 minutes of heating (about 615°C). It can further be mentioned that at temperatures greater than the just mentioned 615°C, the linear volume change is changing differently than before – for the natural basalt, it's again increasing slightly lower, while for the basalt product, it increases faster. The comparison of natural basalt and basalt product with their corresponding temperatures can be seen in Fig. 4.28.

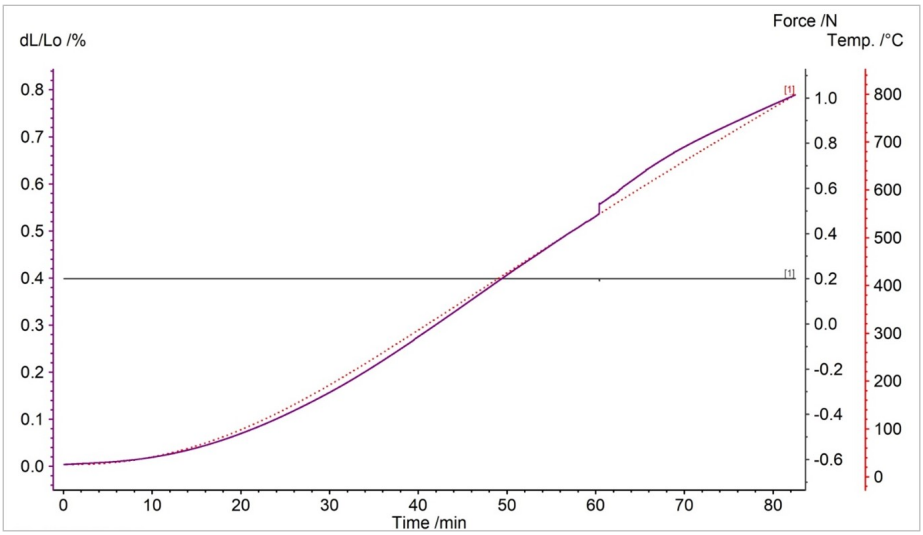

Figure 4.26: Plot of the dilatometric measurement of the natural basalt (Created with NETZSCH Proteus software).

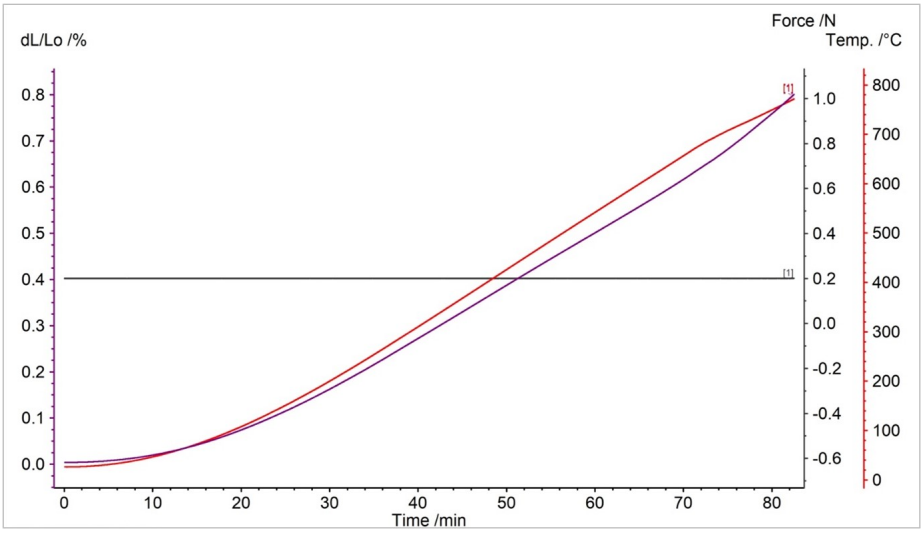

Figure 4.27: Plot of the dilatometric measurement of the cast basalt (Created with NETZSCH Proteus software).

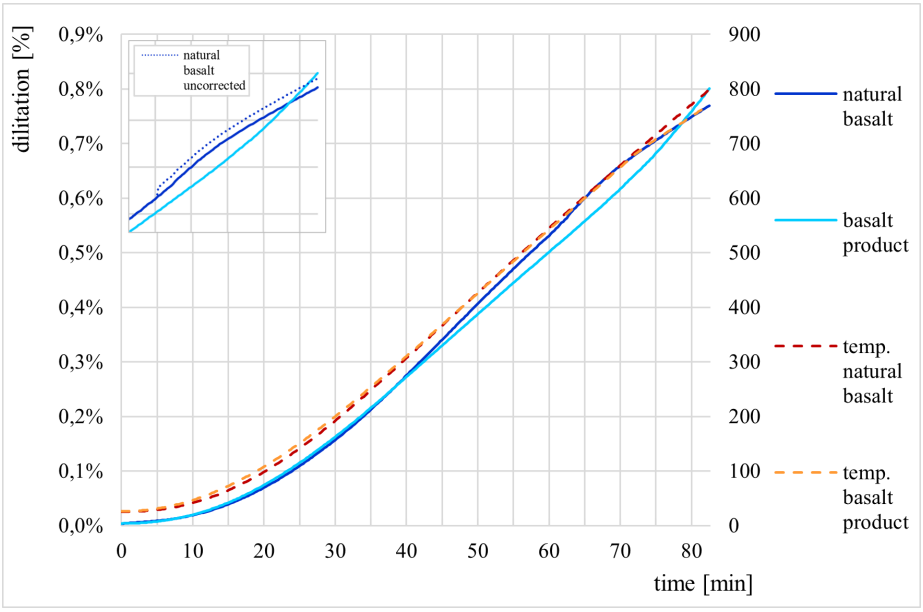

Figure 4.28: Change of length and temperature during the dilatometric measurement for natural and cast basalt.

Chapter 5

Comparison of packed and fluidized bed thermal energy storage

With nearly all research focused on variations and combinations of packed bed and liquid storage, this work also investigates a more rare option of storing heat in solid material. The accumulation of heat in a fluidized bed.

The question answered in this chapter is whether a fluidized bed offers advantageous qualities for storing thermal energy compared to a packed bed. This part of the dissertation veers away from rock pieces and steers towards grain to sand-sized material. By measuring the temperature distribution and pressure drop within the storage vessel, the charging behaviour of the packed and fluidized bed is described and compared. A novel concept using multiple fluidized beds as a flexible storage unit is presented.

5.1 Materials

Technical sand (ST 03/30) was selected for this preliminary exploration, as it is a widely available rock and easy to handle for fluidization. In addition, the fluidization properties (including mean diameter and sphericity) of another basalt product were determined.

5.1.1 Chemical composition of ST 03/30

The sand was bought from the company Sklopísek Střeleč and consists mainly from Silicon dioxide, see Table 5.1 [10].

Table 5.1: Chemical components of ST 03/30 [10]

ST 03/30	
SiO_2	99.2 %
Fe_2O_3	0.1 %

With our analysis (Fig. 5.1), the sands' chemical composition as given in the company's data sheet could be confirmed. ST 03/30 before and after cycling is represented by sand 1 (black) and 3 (red), respectively, while ST 05/10 is marked as sand 2 (blue). The analysis further shows that no chemical composition changes due to heating the sand.

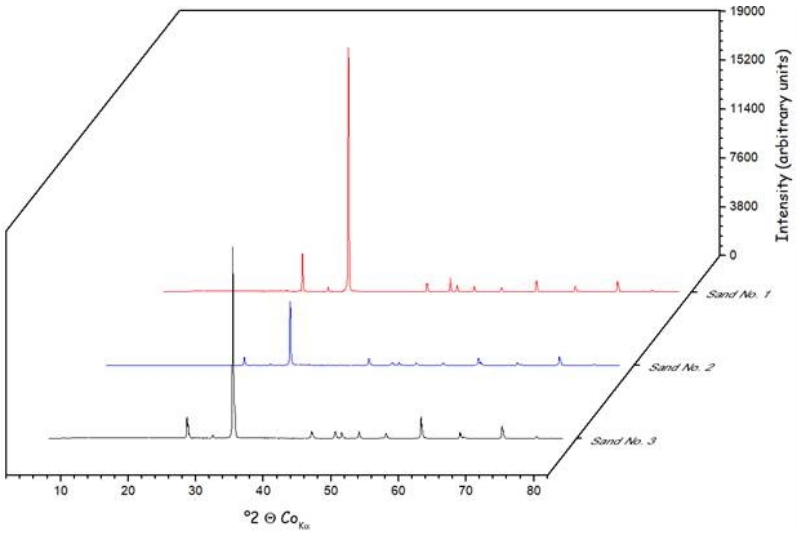

Figure 5.1: Chemical composition of ST03/30.

5.1.2 Chemical composition of the basalt product for fluidization

The basalt product used for the fluidization analysis is a waste by-product of the production of the cast basalt product. The chemical composition was analysed for this thesis in cooperation with Kai Knobloch of the DTU, using SEM/EDS analysis. Compared to the sand, the basalt product for fluidization has oxygen and silicon as main components and higher amounts of carbon, magnesium, iron, and aluminium.

Table 5.2: EDS analysis of the basalt product for fluidization. in mass percent of elements as average of 250x and 400x image with three identified main sections.

Sample area	**section 1/3**	**section 2/3**	**section 3/3**
Oxygen	51,59	49,46	34,82
Carbon	8,27	5,05	63,67
Magnesium	18,18	5,31	0,18
Silicon	13,79	19,21	0,49
Iron	6,36	4,71	0,06
Aluminium	0,91	6,91	0,19
Sodium	0,53	2,85	0,28
Calcium	1,00	6,52	0,33

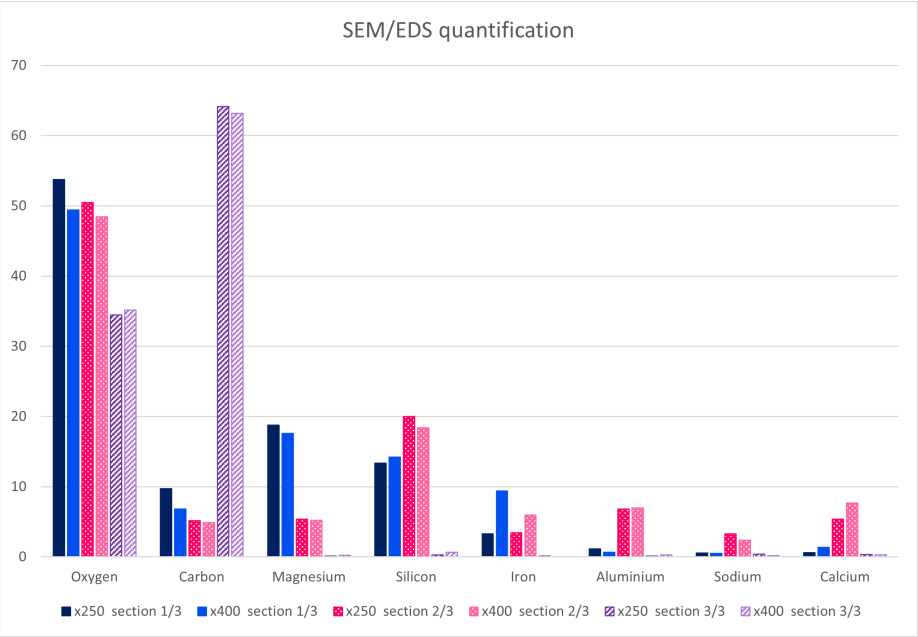

Figure 5.2: Graphical representation of the EDS analysis of the basalt product.

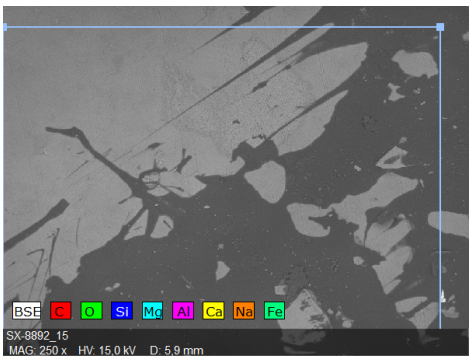

(a) SEM image x250.

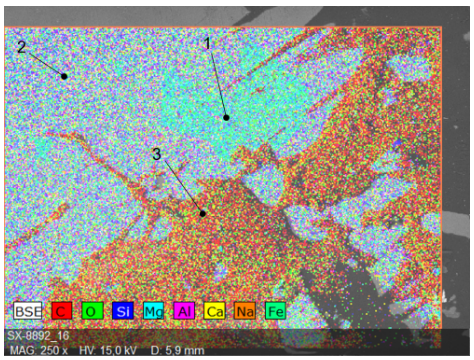

(b) Identified sections 1 to 3 at x250.

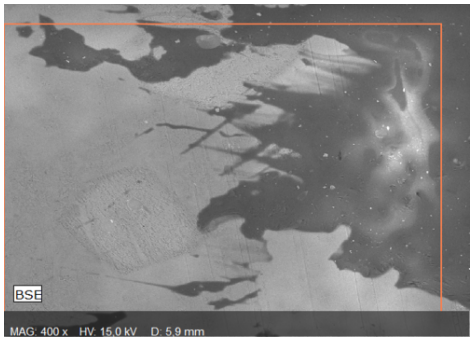

(c) SEM image x400.

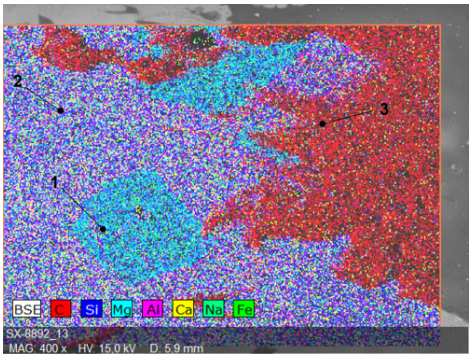

(d) Identified sections 1 to 3 at x400.

Figure 5.3: SEM/EDS images and their identified three main sections.

5.1.3 Fluidization properties

Knowing the minimum fluidization velocity is crucial. For the packed bed, the velocity through the storage material needs to be under the minimum fluidization velocity at all temperatures, and for the fluidized bed, it needs to be well above. The minimum fluidization velocity is calculated according to the following equation (5.1) from Kunii et al. [73].

$$\frac{1.75}{\varepsilon_{mf}^3 \phi_s}(\frac{d_p u_{mf} \rho_g}{\mu})^2 + \frac{150(1-\varepsilon_{mf})}{\varepsilon_{mf}^3 \phi_s^2}(\frac{d_p u_{mf} \rho_g}{\mu}) = \frac{d_p^3 \rho_g (\rho_s - \rho_g) g}{\mu^2} \tag{5.1}$$

The variables of (5.1) are described and given in Table 5.4 for ST 03/30 and in Table 5.5 for basalt. The minimum fluidization velocity of the sand used for the comparison of the packed and fluidized bed is shown in Fig. 5.4 and, in comparison with the basalt product, in Fig. 5.6.

5.1.3.1 ST 03/30

Table 5.3 are the values given by the company for St 03/30. For the fluidization of the material, the mean diameter is an important value. As the sand is usually not used for such an appliance, the value might be sufficiently accurate. Therefore, the particle distribution was separately analysed, and a mean diameter of 0.8 mm was determined (instead of 1.7 mm in the datasheet). The sphericity was found experimentally by determining the minimum fluidization velocity in a non-insulated, plexiglass version of the *mini-fluid*.

Table 5.3: Mean diameter and density of ST 03/30 [10]

ST 03/30		
d_p $(= d_{mean})$	m	0.0017
ρ_s	kg/m^3	2650

Based on the minimum fluidization velocity calculation, an air velocity of 0.3 m/s was selected for the packed bed and an air velocity of 0.7 m/s for the fluidized bed. Like this, the air velocity stays under the lowest minimum fluidization velocity reached during heating (minimum fluidization velocity at $227°C$ is 0.36 m/s) and above the highest minimum fluidization velocity (0.43 m/s at $27°C$), guaranteeing, a packed and fluidized bed structure, respectively.

Table 5.4: Fluidization properties of ST03/30 [11]

Sand type			**ST03/30**		
T	temperature	°C	27	127	227
a	width	m	0.15	0.15	0.15
b	depth	m	0.225	0.225	0.225
A	crossflow area	m^2	0.03375	0.03375	0.03375
g	gravity constant	m/s^2	9.81	9.81	9.81
d_p $(= d_{mean})$	particle diameter	m	0.0008	0.0008	0.0008
ϕ_s	sphericity sand	-	0.83	0.83	0.83
ε_{mf}	void fraction	-	0.4340	0.4340	0.4340
μ	dynamic viscosity	$kg/(m \cdot s)$	0.00001846	0.00002286	0.0000267
ρ_g	air density	kg/m^3	1.176	0.882	0.705
ρ_s	sand density	kg/m^3	2650	2650	2650
ρ_b	sand bulk density	kg/m^3	1500	1500	1500
u_{mf}	min. fl. velocity	m/s	0.43	0.40	0.36
$\dot{V}$	min. fl. volume flow	m^3/h	52.67	48.43	44.34

Figure 5.4: Minimum fluidization velocity of the sand ST 03/30 (violet area marks the temperature range used in the storage).

5.1.3.2 Basalt product

The mean diameter of the basalt product for fluidization is 2.27 mm, also determined with particle size analysis (granulometry). The particle size distribution for the basalt is very wide, as can be seen in Fig. 5.5. With a sphericity of 0.59, which is a lot lower than for the sand, and a much higher density and void fraction, the minimum fluidization velocity of the basalt product (Table 5.5) is, on average, about six times higher than for the sand ST

03/30 (Fig. 5.6). However, due to various reasons, the fluidization of the basalt product is not as straightforward as the fluidization of the sand and will be further discussed in chapter 5.5.

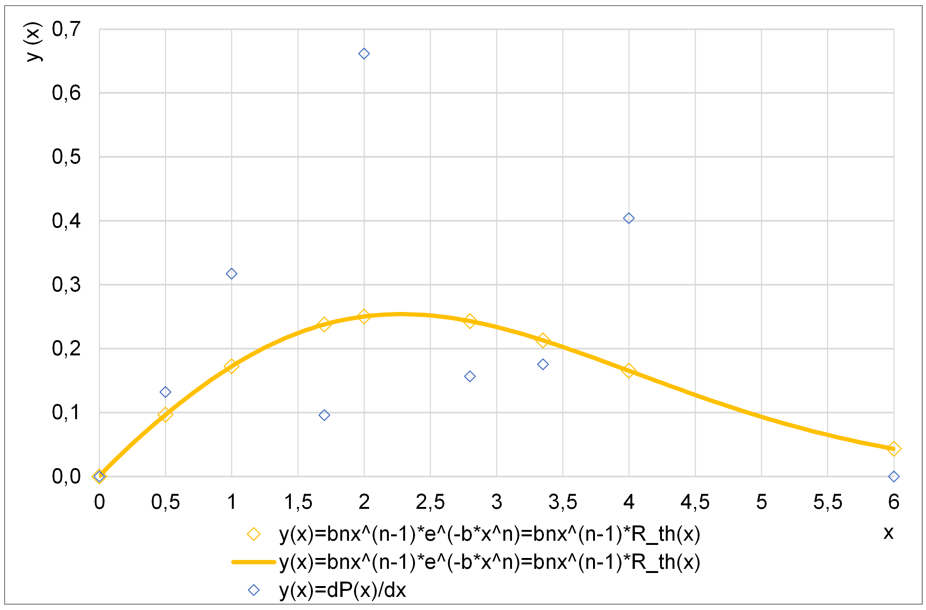

Figure 5.5: The relative percentage frequency curve of the analysed basalt product.

Table 5.5: Fluidization properties of the basalt product for fluidization.

Basalt product for fluidization					
T	temperature	°C	27	127	227
a	width	m	0.15	0.15	0.15
b	depth	m	0.225	0.225	0.225
A	crossflow area	m^2	0.03375	0.03375	0.03375
g	gravity constant	m/s^2	9.81	9.81	9.81
d_p $(= d_{mean})$	particle diameter	m	0.0027	0.0027	0.0027
ϕ_s	sphericity sand	-	0.59	0.59	0.59
ε_{mf}	void fraction	-	0.6278	0.6278	0.6278
μ	dynamic viscosity	$kg/(m \cdot s)$	0.00001846	0.00002286	0.0000267
ρ_g	air density	kg/m^3	1.176	0.882	0.705
ρ_s	basalt density	kg/m^3	3025	3025	3025
ρ_b	basalt bulk density	kg/m^3	1126	1126	1126
u_{mf}	min. fl. velocity	m/s	2.23	2.51	2.72
$\dot{V}$	min. fl. volume flow	m^3/h	271.13	304.37	330.81

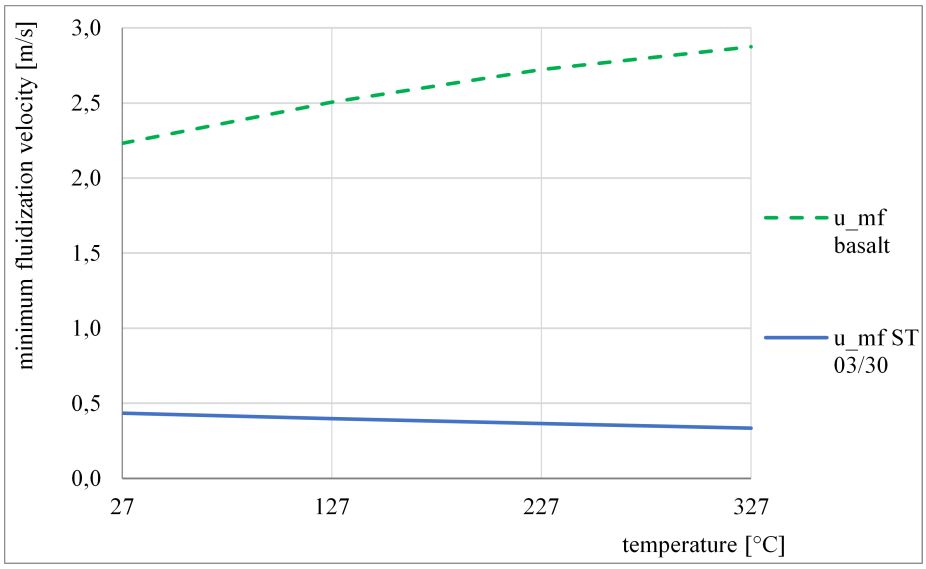

Figure 5.6: Minimum fluidization velocity of the basalt product in comparison to the minimum fluidization velocity of the sand ST 03/30

5.2 Experimental procedure and methodology

The experimental set-up is called the *mini-fluid* (see pictures in Fig. 5.7a and 5.7b). As already mentioned in the last section (5.1.3), the experiment is conducted at an air velocity of 0.3 m/s for the packed bed and at 0.7 m/s for the fluidized bed.

(a) Left.

(b) Front.

Figure 5.7: Pictures of the fluidized bed laboratory set-up

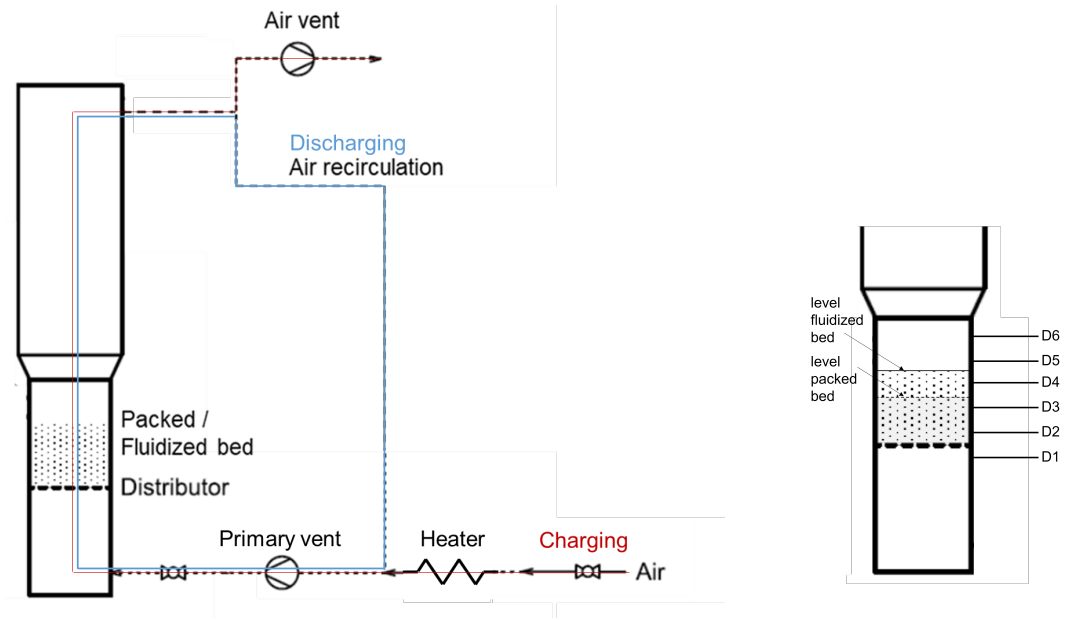

(a) Scheme of the *mini-fluid*. (b) Sensors D1 to D6.

Figure 5.8: Scheme of the laboratory set-up, adapted from [9].

For charging, the air is drawn in from the environment, heated and blown through the thermal storage bed (red path in Fig. 5.8a), before leaving the appliance. For discharging, the air is recirculated and not heated (blue path Fig. 5.8a). This way of cooling with the exiting air is slower as the exiting air has a higher temperature than the surrounding air. A different way of cooling is not possible, as the experiment is also used for different experiments involving combustion. Temperature sensor D1 measures the temperature of the air directly before the distributor, sensors D2 and D3 are in the middle of the packed and fluidized bed, while D4 is still partially immersed in the fluidized bed, but not the packed bed, and D5 and D6 measure the temperature of the air behind the bed (Fig. 5.8b).

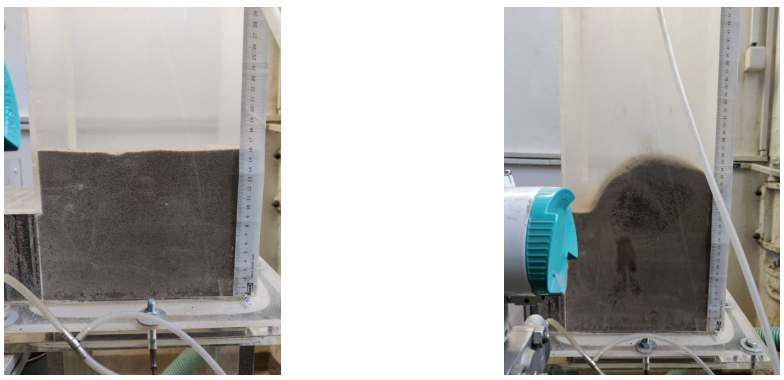

(a) Packed bed. (b) Fluidized bed.

Figure 5.9: Packed and fluidized bed of sand ST 03/30 in the plexi glass *mini-fluid*.

A total mass of 8.1 kg ST 03/30 is used for the experiments. The amount was selected according to the position of the temperature sensors, placing D2 and D3 within the storage bed. For the packed bed, this means a height of 16 cm (Fig.5.9a), while the fluidized bed can bubble up to 25 cm (Fig.5.9b).

5.3 Comparison of ST 03/30 packed and fluidized bed behaviour

The quantitative results of charging and discharging the packed and fluidized bed are only to be seen in comparison and are not transferable due to the *mini-fluids'* specific layout.

5.3.1 Charging behaviour

The fluidized reaches slightly higher mean temperatures during charging (the mean temperature of the temperature sensors D2 and D3 was chosen for comparison, Fig. 5.10). After one hour, the mean temperature of the fluidized bed is 1.67°C higher than the packed bed mean temperature (Table 5.6).

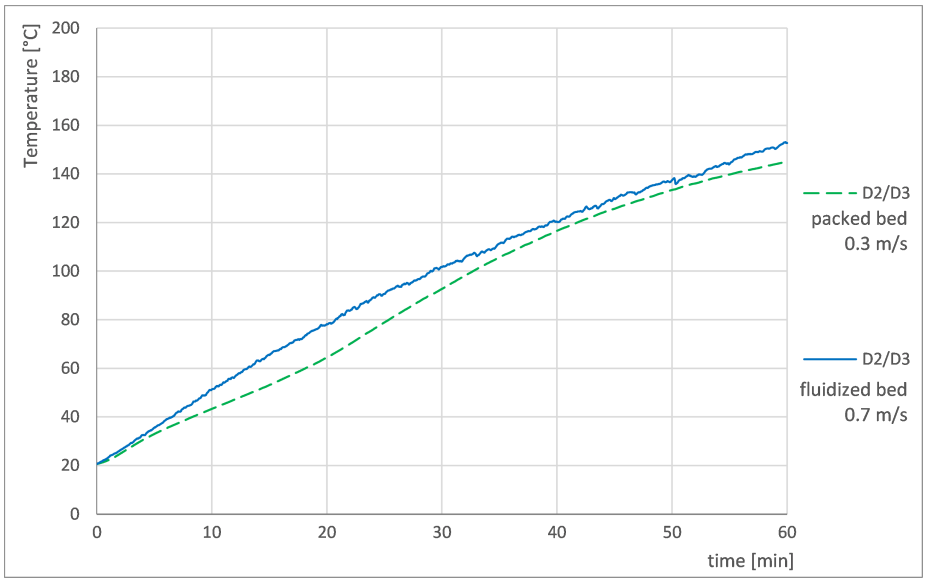

Figure 5.10: Charging behaviour of the packed and fluidized beds over 60 minutes with the mean temperature of the storage

Table 5.6: Temperatures of the packed and fluidized bed after 60 minutes

Packed bed			**Fluidized bed**		
D2	D3	D2/D3 mean	D2	D3	D2/D3 mean
179,61	91,89	135,75	131,73	143,11	137,42

The different characteristics of the packed and fluidized bed can be seen in Fig.5.11 and 5.12. The packed bed has a temperature front moving through the storage (see also Fig.2.8 in chapter 2.2.2), whereas the fluidized bed behaves like a well-mixed fluid.

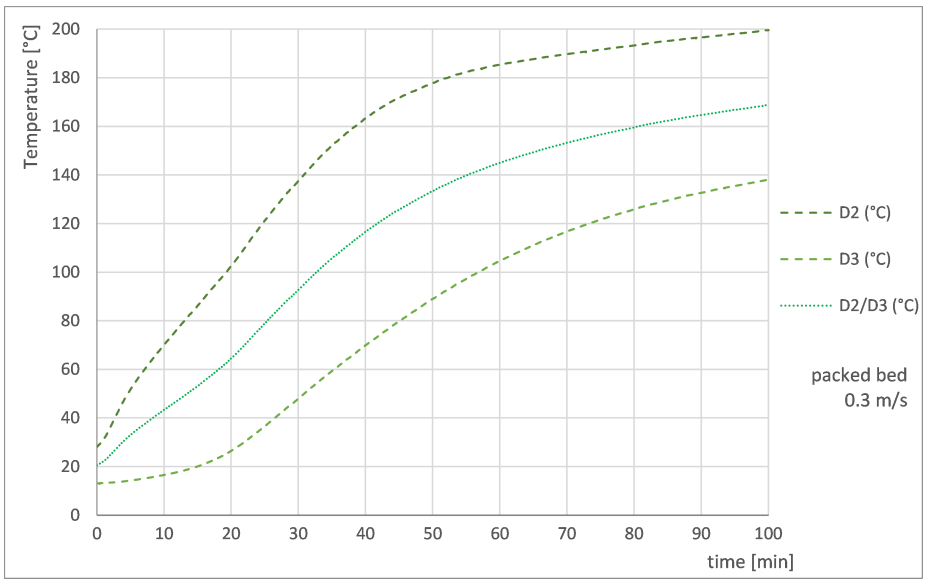

Figure 5.11: Charging behaviour of the packed bed up to a mean temperature of 168.8°C

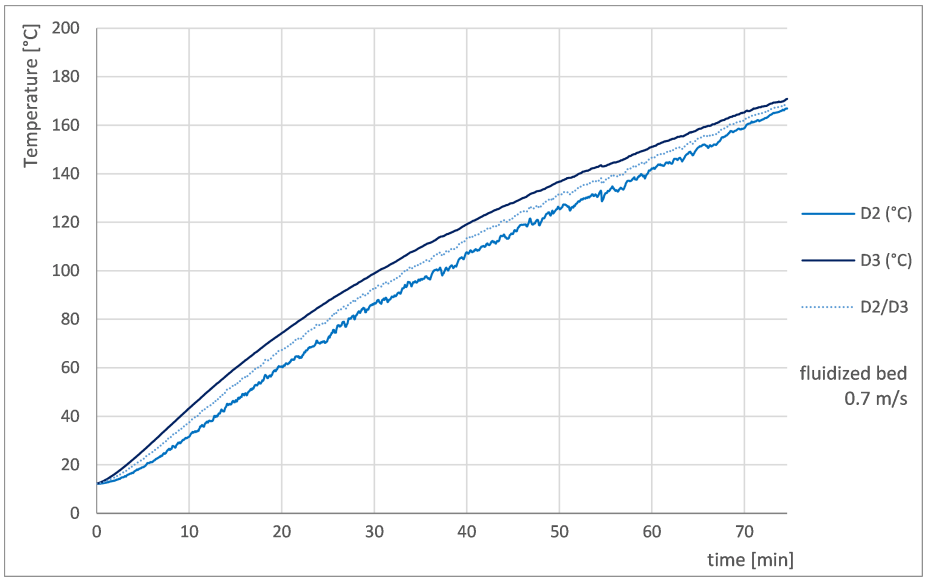

Figure 5.12: Charging behaviour of the packed bed up to a mean temperature of 168.8°C

The packed bed storage needs about 1h 40 m 3 s to reach a mean temperature of D2 and D3 of 168.8°C. The fluidized bed is faster and reaches 168.8°C already after 1 h 15 m 49 s. The maximum temperature in the packed bed storage is then 199.6°C, while only

168.9°C in the fluidized bed storage. While the fluidized bed's maximum and minimum temperature after 1 h 15 m 49 s is 170.8°C and 166.9°C respectively, the packed bed's temperatures after the same time are 191.8°C and 122.3°C with a mean temperature of 157.0°C.

For 16 minutes, until the fluidized bed has reached an average temperature of 55.7°C, the heat flux from air to sand is higher for the fluidized bed than for the packed bed (Fig. 5.13). Above this temperature, the heat flux of the fluidized bed stays approximately constant while it continues to increase for the packed bed. Therefore, also the packed bed's efficiency increases until it stabilises after approximately 45 minutes when the bed reaches about 130°C mean temperature. The total energy stored after 60 minutes (with the internal losses neglected and assuming external losses to be similar for packed and fluidized bed) is 4.07 kJ for the packed bed and 2.59 kJ for the fluidized bed. The fluidized bed has 64 % of the packed beds capacity at a fixed storage time of one hour.

At the same temperature (168.8°C), the packed bed has a storage capacity of 7.65 kJ and the fluidized bed 3.04 kJ (40 % of the packed beds capacity). However, the packed bed needs 25 minutes longer to reach this temperature.

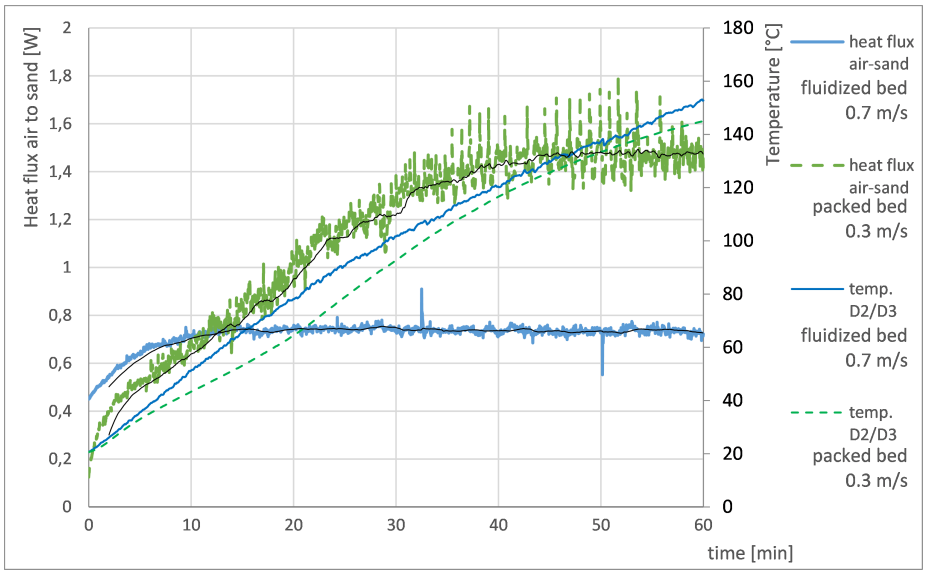

Figure 5.13: Heat flux from the working fluid (air) to the storage material (sand), including a moving average for the heat fluxes to visualise their stabilisation. The according temperatures are also in the diagram for direct comparison

At the end of the charging analysis, the pressure drop within the storage vessel should be shortly addressed. It is measured as the difference of pressure before and after the bed. The pressure drop in the packed is (in average) nearly constant, while it is slightly increasing with higher temperatures (longer charging time) in the fluidized bed (Fig. 5.14. The fluctuation of the pressure drop can be seen in Fig. 5.15.

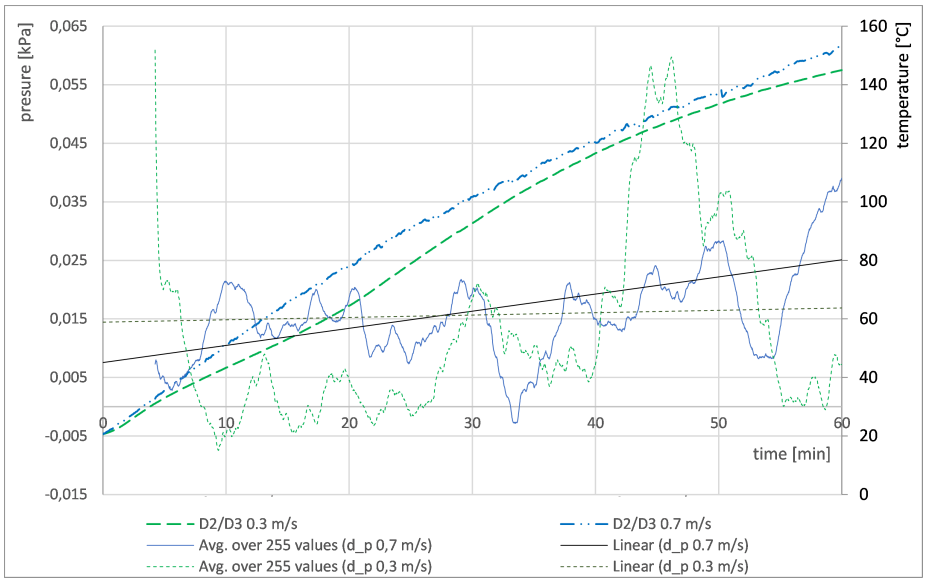

Figure 5.14: Average over 255 values and linear approximation of the pressure drop in the packed and fluidized bed during charging with the mean temperatures.

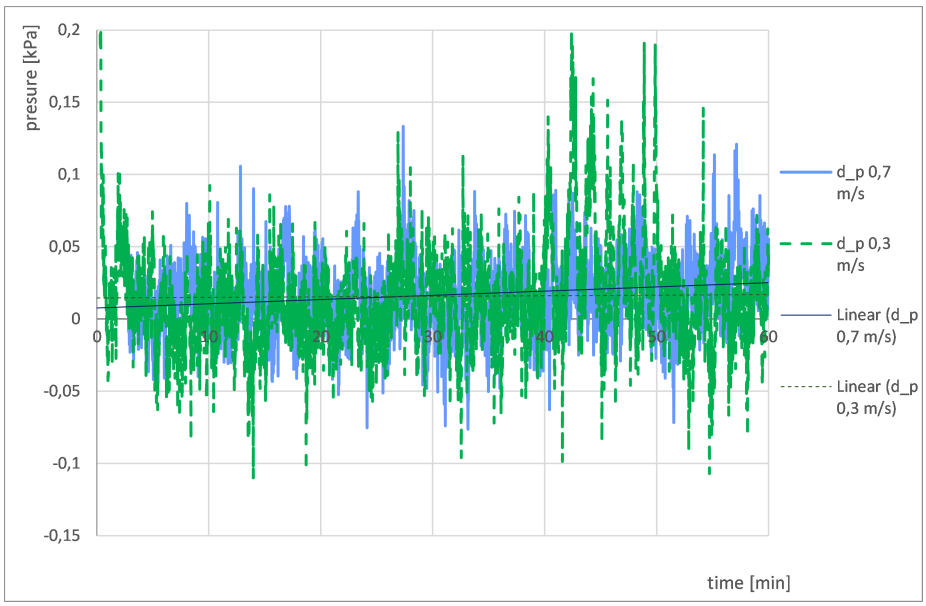

Figure 5.15: Real pressure drop with linear approximation.

Based on this analysis, it can be confirmed that packed beds offer better thermal storage properties when employing a single storage vessel. The packed bed stores a greater amount of energy at a faster rate (higher heat flux from air to sand) but a slightly lower mean temperature after the same time. The use of a single fluidized bed for energy storage is, therefore, of limited use only despite its slightly faster charging. A fluidized bed behaves like a well-mixed storage and provides a continuously changing temperature output, while the

temperature output of a packed bed is relatively constant, a key property for most technical machinery. In thermal energy storage appliances, the goal is to have a steep temperature front in the packed bed storage. This means that heat dissipation or additional heat provision is necessary to provide a constant temperature output for fluidized bed storage. This is essential for the use of the energy storage in a Carnot battery or any kind of power-to-heat process, as well as for the direct use for heating, etc. In chapter 5.4, a novel idea to limit these negative effects is discussed. The proposal is a multi-layered fluidized bed, artificially creating a temperature stratification throughout the storage.

5.3.2 Discharging behaviour

The fluidized bed is discharged a lot faster than the packed bed. However, this might be because a packed bed would usually be discharged with airflow in the opposite direction. The effect caused by discharging in the same direction can be seen in Fig.5.18. The temperature front is first continuing to move through the storage, heating the colder sand and turning around the temperature distribution in the storage (see blue arrow in diagram) before starting to cool down with a temperature front moving again through the bed. A deeper analysis of the discharging behaviour wouldn't bring useful results, as the set-up of the *mini-fluid* doesn't allow the use of fresh air for cooling but only recirculated air. Further, the results of temperature sensor D1, are influenced by the heat radiating from the heated distributor.

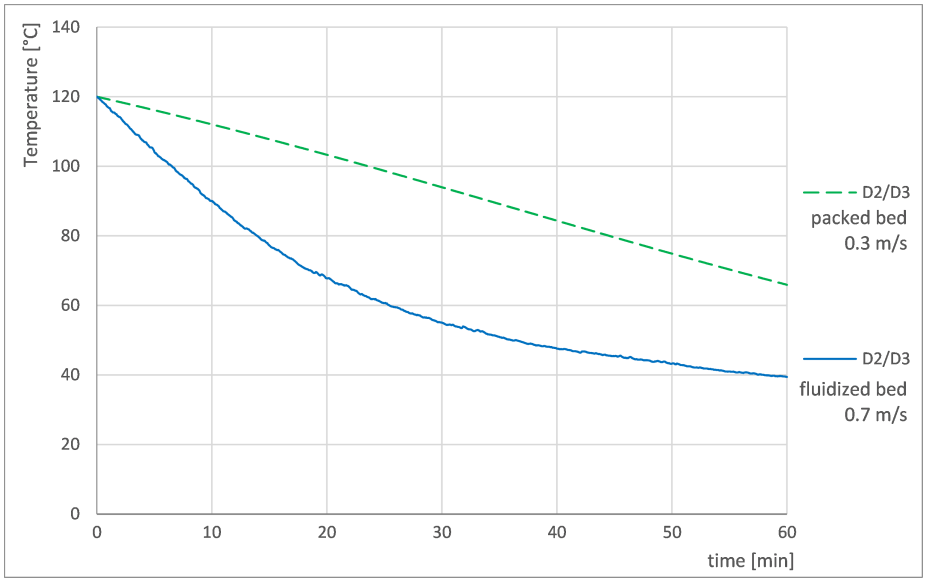

Figure 5.16: Discharging behaviour of the packed and fluidized beds over 60 minutes, after "turn" of the temperature front, with the mean temperature of the storage

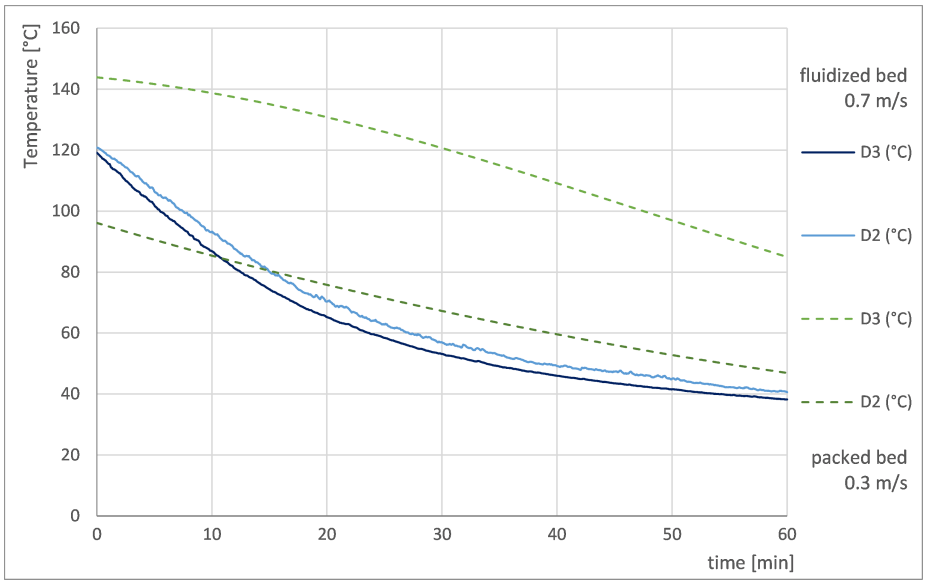

Figure 5.17: Discharging behaviour of the packed and fluidized beds over 60 minutes, after "turn" of the temperature front.

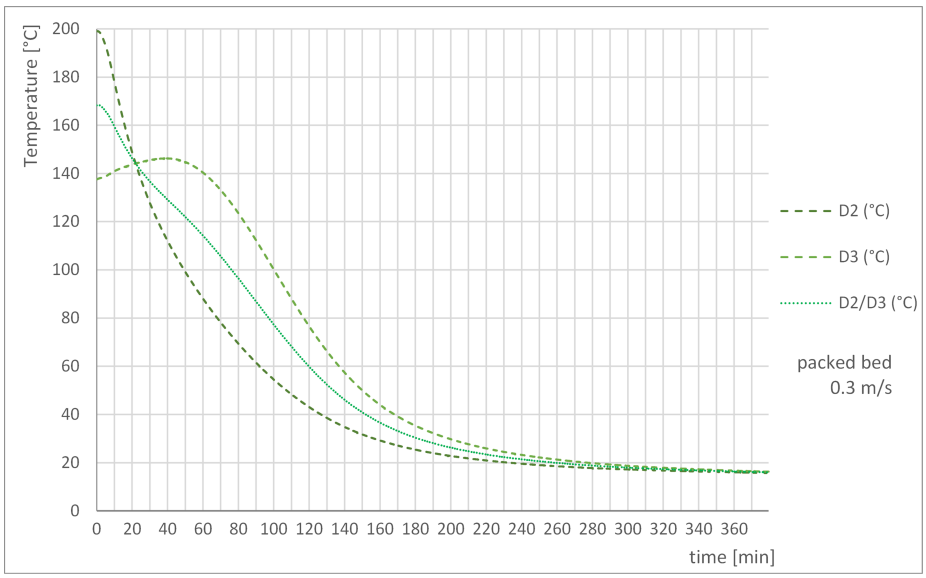

Figure 5.18: Discharging behaviour of the packed bed and "turn" of temperature front, because of discharging in the same direction like charging.

5.4 Model of a multi-layered fluidized bed storage

At the end of the analysis of the packed and fluidized bed charging behaviour in chapter 5.3.1 the conclusion was that a single fluidized bed cannot compete with a single packed bed due to a lower heat transfer rate and an unknown output temperature. Artificially

creating temperature layers within the fluidized bed by separating it into multiple beds would help minimise the latter. A multi-layered fluidized bed would offer the new advantage of being a flexible storage unit, which can be adjusted to the desired output temperature (total temperature difference in the storage). A possible constellation of 4 fluidized beds, reaching also a temperature difference of 146°C can be seen in Fig. 5.19 and 5.20.

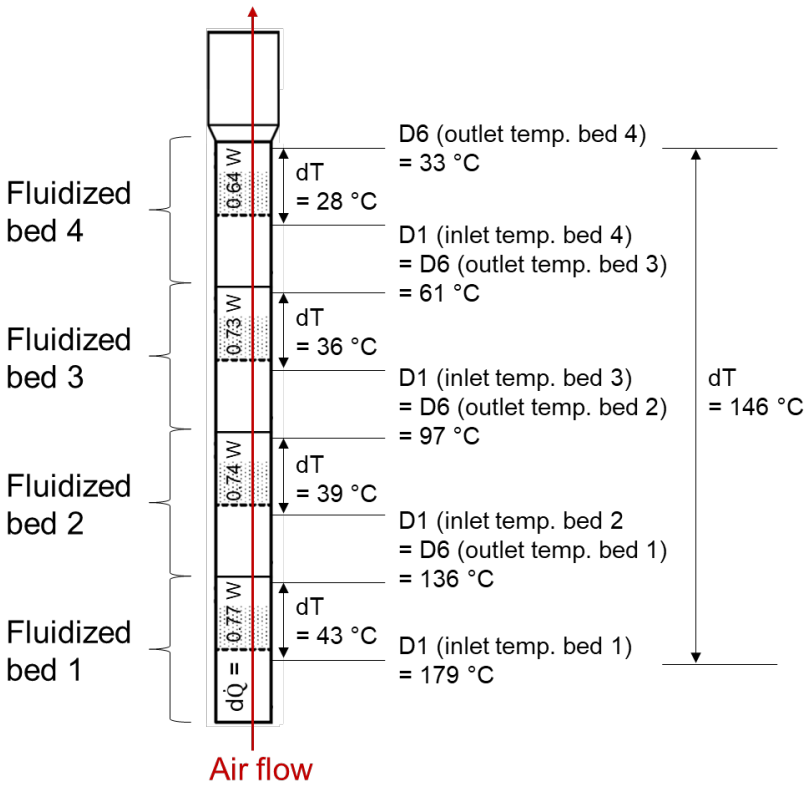

Figure 5.19: Scheme of a multi-layered fluidized bed with four layers, temperature difference 146°C and approximately constant heat flux.

This option of multiple layers of fluidized bed storage offers great flexibility and a better prediction of the output temperature while always employing the maximal possible heat flux in the fluidized bed. The main downside is that a fluidized bed has a higher energy consumption than a packed bed due to the necessary higher velocities of the working fluid, reducing the round-trip efficiency of a Carnot battery deploying it. Further, the distributor before the bed has a pressure drop of 0.3 kPa, while the fluidized bed storage itself has only a pressure drop staying under 0.05 kPa to 0.1 kPa. By separating the storage into multiple beds, it needs to be taken into account that each bed will have the pressure drop of its distributor, increasing the power consumption. Each bed and connecting pipe between the beds will have losses to the environment, needs material to be built, insulation, storage material, and space. It is questionable if this concept has a use case when similar behaviour of four fluidized beds can be achieved with one to two packed beds.

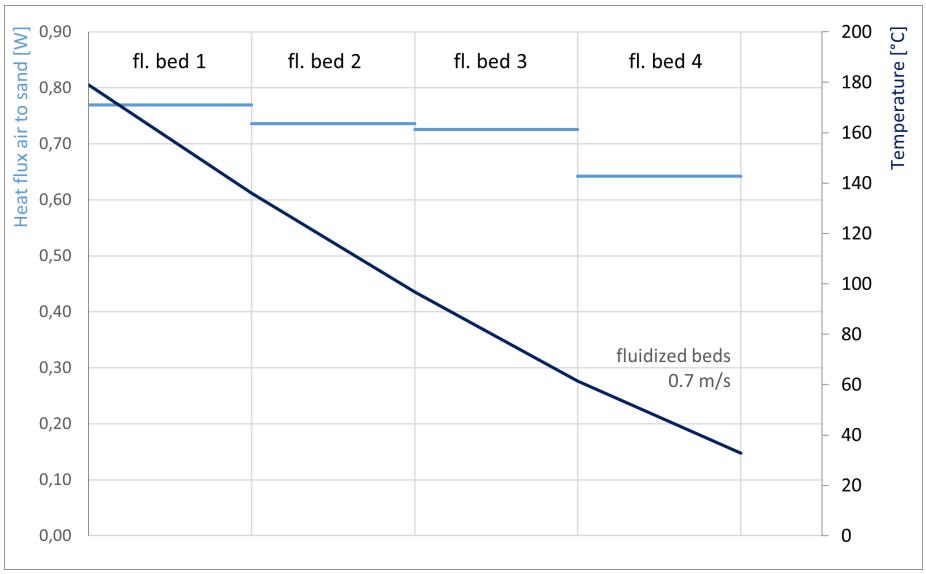

Figure 5.20: Multi-layered fluidized bed with four layers, temperature difference 146°C and approximately constant heat flux.

5.5 Notes to a theoretical fluidized bed concept with basalt

The chemical composition of the basalt product for fluidization was described in chapter 5.1.2. For similar, theoretical fluidization results like the basalt product with a determined mean diameter of 2.74 mm is sand with a diameter of 2.42 mm (see Table 5.7).

Table 5.7: Equivalent diameter of sand for the used basalt rock pieces

basalt		
$d_{p,b}$ $(= d_{50})$	m	0,00274
$\phi_{S,b}$	-	0.59
ρ_b	kg/m^3	3025
$a_{V,b}$	m	$1.07709 \cdot 10^{-8}$
$a_{S,b}$	m	$3.9976 \cdot 10^{-5}$
$a_{VS,b}$	-	$7.81903 \cdot 10^{-16}$
sand ST 03/30		
ρ_s	kg/m^3	2650
$a_{VS,b}$	-	$8.35397 \cdot 10^{-16}$
ϕ_{S_s}	-	0.83
$d_{p,s}$ $(= d_{50})$	m	0.00242

These results allow an analysis of the basalt's behaviour with the use of the equivalent sand, as done in chapter 5.1.3.2. However, it is questionable if fluidization of the waste

basalt material is possible. With 1.9 kg basalt product in the *mini-fluid*, fluidization wasn't achieved (Fig. 5.21a). At a velocity of $125 m^3/h$ the bed showed fountains (see Fig. 5.21b). The calculated minimum fluidization volume flow at room temperature is $271 m^3/h$. This is about five times higher than, in comparison, ST 03/30, which has a minimum fluidization volume flow of $53 m^3/h$. Besides the high minimum fluidization velocity, the wide particle size distribution and the sharp-edged, unregular shape of the particles, classified as Geldart D, are two more problems for fluidization. Through their shape, the particles block each other, causing the fountains.

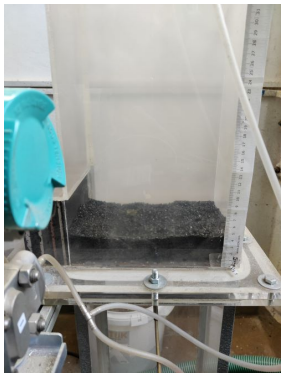

(a) Packed bed.

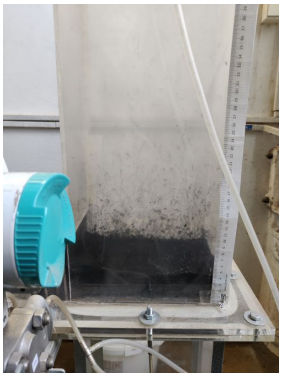

(b) Bed with fountains.

Figure 5.21: Packed bed and bed with fountains (no fluidization, even at high air velocity) of waste basalt in the plexi glass *mini-fluid*.

Chapter 6

Summary and Conclusion

This dissertation thesis governs the state-of-the-art on Carnot batteries, describes the behaviour of basalt at high temperatures and compares the accumulation of heat in packed and fluidized beds.

6.1 Summary

In the first chapter of this thesis (1), it is pointed out that Carnot batteries are an important part of the development to a greener future, deploying renewable energy sources and the underlying problem was explained. In chapter 2, Brayton cycle, Rankine cycle and electric heater Carnot battery layouts are introduced and the different thermal storage possibilities outlined. Following a summary of the different Carnot battery layouts in the literature, ongoing projects, lab-scale demonstrators and pilot plants are introduced. At the end of the chapter, various storage materials are presented, and basalt is outlined as the rock to be investigated in this work. This leads to the next chapter (4), where the behaviour of basalt at high temperatures for use in thermal storage is analysed and assessed. The speed of the specific heat capacity is modelled based on calorimetric experiments and material changes due to heating, particularly surface alterations, density deviations and dilatometric variations. Basalt is a useful material for packed bed thermal storage, with minor degradation due to cycling. The comparison of packed and fluidized bed thermal storage in chapter 5 was done with sand and shows that packed beds offer better thermal storage performance for a one vessel set-up. A multi-layered fluidized bed is suggested as a theoretical concept to exploit the benefits of both packed and fluidized beds. Fluidization of basalt material was not achieved and is ruled to be difficult, if not entirely impossible.

6.2 Conclusion

This thesis describes natural and cast basalt behaviour in packed bed thermal storage for Carnot batteries and suggests a novel concept with a multilayered fluidized bed thermal storage for Carnot batteries.

The **objectives** and **tasks** listed in chapter 3 on page 17 have the following outputs:

1. Experiments and mathematical model of the speed of reaching the full potential heat capacity of natural and cast basalt

   ⇒ Natural and cast basalt's charging and discharging behaviour is described, using mathematical models of the specific heat capacity over time and temperature. A small decrease in heat capacity due to repeated heating is observed.

   ⇒ Basalt and cast basalt are very good thermal energy storage materials. Natural basalt is a material with low environmental impact. Waste cast basalt products can be recycled and re-purposed after the original intended use.

2. Complementing experiments with natural and cast basalt (density determination, dilatometry, evaluation of surface changes)

   ⇒ Small changes of length, density and surface were observed. The decrease in heat capacity coincides with these results.

3. Experiments on packed and fluidized bed thermal storage

   ⇒ A single vessel packed bed storage offers better thermal storage properties than a single fluidized storage vessel.

   ⇒ Multilayered fluidized bed storage theoretically offers the benefits of packed and fluidized bed storage and more flexibility compared to simple packed bed storage. However, it is a more complicated set-up with probably low overall efficiency.

   ⇒ Basalt seems to be unsuitable for fluidization.

6.3 Outlook

The following is suggested to be explored further:

- It would be interesting to investigate another possibility of determining the heat capacity of rocks or complete set-ups. The idea would be to place them in a furnace, measuring the appliance's power consumption and using it to draw conclusions about heat capacity.

- Considering other natural storage materials, like diabase or magnetite, and directly comparing them to basalt, would allow specific assessment of their use and application range.
- The concept of the multilayered fluidized bed could be analyzed further, considering thermodynamic and flow losses, and tested in a specific experimental set-up.
- Knowing that basalt is a great thermal storage material and how it specifically behaves, allows better planning of a Carnot battery storage system. The acquired information can also be used to enhance storage and system simulation.

Bibliography

[1] LB MINERALS. 2014.

[2] Waples, D. W.; Waples, J. S. A Review and Evaluation of Specific Heat Capacities of Rocks, Minerals, and Subsurface Fluids. Part 1: Minerals and Nonporous Rocks. *Natural Resources Research*, volume 13, no. 2, 2004: pp. 97–122, ISSN 1520-7439, Doi: 10.1023/B:NARR.0000032647.41046.e7.

[3] Becattini, V.; Motmans, T.; Zappone, A.; et al. Experimental investigation of the thermal and mechanical stability of rocks for high-temperature thermal-energy storage. *Applied Energy*, volume 203, 2017: pp. 373–389, ISSN 03062619, Doi: 10.1016/j.apenergy.2017.06.025.

[4] Martin, C.; Breidenbach, N.; Eck, M. Screening and Analysis of Potential Filler Materials for Molten Salt Thermocline Storages. In *Proceedings of the ASME 8th International Conference on Energy Sustainability - 2014*, New York, NY: ASME, 2014, ISBN 978-0-7918-4586-8, Doi: 10.1115/ES2014-6493.

[5] Hartlieb, P.; Toifl, M.; Kuchar, F.; et al. Thermo-physical properties of selected hard rocks and their relation to microwave-assisted comminution. *Minerals Engineering*, volume 91, 2016: pp. 34–41, ISSN 08926875, Doi: 10.1016/j.mineng.2015.11.008.

[6] Nahhas, T.; Py, X.; Sadiki, N. Experimental investigation of basalt rocks as storage material for high-temperature concentrated solar power plants. *Renewable and Sustainable Energy Reviews*, volume 110, 2019: pp. 226–235, ISSN 13640321, Doi: 10.1016/j.rser.2019.04.060.

[7] Katedra materiálového inženýrství a chemie, FSv, ČVUT v Praze. Helium pycnometer. 2019. Available from: `https://k123.fsv.cvut.cz/en/helium-pycnometer/`

[8] Katedra materiálového inženýrství a chemie, FSv, ČVUT v Praze. Vysokoteplotní dilatometr DIL 402 Expedis select. 2019. Available from: `https://k123.fsv.cvut.cz/vysokoteplotni-dilatometr-dil-402-expedis-select/`

[9] Vodička, M.; Michaliková, K.; Hrdlička, J.; et al. External bed materials for the oxy-fuel combustion of biomass in a bubbling fluidized bed. *Journal of Cleaner Production*, volume 321, 2021: p. 128882, ISSN 09596526, Doi: 10.1016/j.jclepro.2021.128882.

[10] Sklopísek Střeleč. Technical sands. 2021. Available from: `https://glassand.eu/celkova-produkce/podle-druhu/technicke-pisky`

[11] Air - Specific Heat vs. Temperature at Constant Pressure. 14.01.2022. Available from: `https://www.engineeringtoolbox.com/air-specific-heat-capacity-d_705.html`

[12] IEA. Czech Republic - Countries & Regions - IEA. 2018. Available from: `https://www.iea.org/countries/czech-republic`

[13] EuropeanUnion. Delivering the European Green Deal. 2021. Available from: `https://ec.europa.eu/info/strategy/priorities-2019-2024/european-green-deal/delivering-european-green-deal_en`

[14] Gallo, A. B.; Simões-Moreira, J. R.; Costa, H.; et al. Energy storage in the energy transition context: A technology review. *Renewable and Sustainable Energy Reviews*, volume 65, 2016: pp. 800–822, ISSN 13640321, Doi: 10.1016/j.rser.2016.07.028.

[15] IEA; International Energy Agency. Technology Roadmap Energy storage. 2014. Available from: `https://www.iea.org/reports/technology-roadmap-energy-storage`

[16] Valera-Medina, A.; Xiao, H.; Owen-Jones, M.; et al. Ammonia for power. *Progress in Energy and Combustion Science*, volume 69, 2018: pp. 63–102, ISSN 03601285, Doi: 10.1016/j.pecs.2018.07.001.

[17] Gil, A.; Medrano, M.; Martorell, I.; et al. State of the art on high temperature thermal energy storage for power generation. Part 1—Concepts, materials and modellization. *Renewable and Sustainable Energy Reviews*, volume 14, no. 1, 2010: pp. 31–55, ISSN 13640321, Doi: 10.1016/j.rser.2009.07.035.

[18] Farres-Antunez, P.; White, A. Optimisation of heat exchangers operating with real fluids for thermo-mechanical energy storage. 2016, Doi: 10.13140/RG.2.2.29926.98885.

[19] McTigue, J. D.; Markides, C. N.; White, A. J. Performance response of packed-bed thermal storage to cycle duration perturbations. *Journal of Energy Storage*, volume 19, 2018: pp. 379–392, Doi: 10.1016/j.est.2018.08.016.

[20] Wang, L.; Lin, X.; Chai, L.; et al. Unbalanced mass flow rate of packed bed thermal energy storage and its influence on the Joule-Brayton based Pumped Thermal Electricity Storage. *Energy Conversion and Management*, volume 185, 2019: pp. 593–602, ISSN 0196-8904, Doi: 10.1016/j.enconman.2019.02.022.

[21] Odenthal, C.; Steinmann, W.-D.; Zunft, S. Analysis of a horizontal flow closed loop thermal energy storage system in pilot scale for high temperature applications – Part II: Numerical investigation. *Applied Energy*, volume 263, 2020: p. 114576, ISSN 03062619, Doi: 10.1016/j.apenergy.2020.114576.

[22] Attonaty, K.; Stouffs, P.; Pouvreau, J.; et al. Thermodynamic analysis of a 200 MWh electricity storage system based on high temperature thermal energy storage. *Energy*, volume 172, 2019: pp. 1132–1143, ISSN 03605442, Doi: 10.1016/j.energy.2019.01.153.

[23] Herrmann, U.; Schwarzenbart, M.; Dittmann-Gabriel, S. Speicher statt Kohle: Integration thermischer Stromspeicher in vorhandene Kraftwerksstandorte. *EnergieForum*, volume 71, no. 4, 2019: pp. 42–45.

[24] Amy, C.; Seyf, H. R.; Steiner, M. A.; et al. Thermal energy grid storage using multi-junction photovoltaics. *Energy & Environmental Science*, volume 12, no. 1, 2019: pp. 334–343, ISSN 1754-5692, Doi: 10.1039/C8EE02341G.

[25] Desrues, T.; Ruer, J.; Marty, P.; et al. A thermal energy storage process for large scale electric applications. *Applied Thermal Engineering*, volume 30, no. 5, 2010: pp. 425–432, ISSN 1359-4311, Doi: 10.1016/j.applthermaleng.2009.10.002.

[26] Davenne, T. R.; Peters, B. M. An Analysis of Pumped Thermal Energy Storage With De-coupled Thermal Stores. *Frontiers in Energy Research*, volume 8, 2020, Doi: 10.3389/fenrg.2020.00160.

[27] Howes, J. Concept and Development of a Pumped Heat Electricity Storage Device. *Proceedings of the IEEE*, volume 100, no. 2, 2012: pp. 493–503, ISSN 0018-9219, Doi: 10.1109/JPROC.2011.2174529.

[28] McTigue, J. D.; White, A. J.; Markides, C. N. Parametric studies and optimisation of pumped thermal electricity storage. *Applied Energy*, volume 137, 2015: pp. 800–811, ISSN 03062619, Doi: 10.1016/j.apenergy.2014.08.039.

[29] Chen, L. X.; Hu, P.; Zhao, P. P.; et al. Thermodynamic analysis of a High Temperature Pumped Thermal Electricity Storage (HT-PTES) integrated with a parallel organic Rankine cycle (ORC). *Energy Conversion and Management*, volume 177, 2018: pp. 150–160, ISSN 0196-8904, Doi: 10.1016/j.enconman.2018.09.049.

[30] McTigue, J. 'Carnot Batteries' for Electricity Storage. 2019. Available from: `https://www.nrel.gov/docs/fy20osti/75559.pdf`

[31] Thermo-electrical energy storage: a new type of large scale energy storage based on thermodynamic cycles. 2011. Available from: `https://www.researchgate.net/publication/259973612_Thermoelectric_energy_storage_a_new_type_of_large_scale_energy_storage_based_on_thermodynamic_cycles`

[32] Abarr, M.; Geels, B.; Hertzberg, J.; et al. Pumped thermal energy storage and bottoming system part A: Concept and model. *Energy*, volume 120, 2017: pp. 320–331, ISSN 03605442, Doi: 10.1016/j.energy.2016.11.089.

[33] Abarr, M.; Hertzberg, J.; Montoya, L. D. Pumped Thermal Energy Storage and Bottoming System Part B: Sensitivity analysis and baseline performance. *Energy*, volume 119, 2017: pp. 601–611, ISSN 03605442, Doi: 10.1016/j.energy.2016.11.028.

[34] Peterson, R. B. A concept for storing utility-scale electrical energy in the form of latent heat. *Energy*, volume 36, no. 10, 2011: pp. 6098–6109, ISSN 03605442, Doi: 10.1016/j.energy.2011.08.003.

[35] Steinmann, W. D. The CHEST (Compressed Heat Energy STorage) concept for facility scale thermo mechanical energy storage. *Energy*, volume 69, 2014: pp. 543–552, ISSN 03605442, Doi: 10.1016/j.energy.2014.03.049.

[36] Mercangöz, M.; Hemrle, J.; Kaufmann, L.; et al. Electrothermal energy storage with transcritical CO 2 cycles. *Energy*, volume 45, no. 1, 2012: pp. 407–415, ISSN 03605442, Doi: 10.1016/j.energy.2012.03.013.

[37] Ayachi, F.; Tauveron, N.; Tartière, T.; et al. Thermo-Electric Energy Storage involving CO2 transcritical cycles and ground heat storage. *Applied Thermal Engineering*, volume 108, 2016: pp. 1418–1428, ISSN 1359-4311, Doi: 10.1016/j.applthermaleng.2016.07.063.

[38] Kim, Y.-M.; Shin, D.-G.; Lee, S.-Y.; et al. Isothermal transcritical CO2 cycles with TES (thermal energy storage) for electricity storage. *Energy*, volume 49, 2013: pp. 484–501, ISSN 03605442, Doi: 10.1016/j.energy.2012.09.057.

[39] Kim, Y. M.; Kim, C. G.; Favrat, D. Transcritical or supercritical CO2 cycles using both low- and high-temperature heat sources. *Energy*, volume 43, no. 1, 2012: pp. 402–415, ISSN 03605442, Doi: 10.1016/j.energy.2012.03.076.

[40] Siemens Gamesa Renewable Energy, S.A. World first: Siemens Gamesa begins operation of its innovative electrothermal energy storage system. 2019. Available from: `https://www.siemensgamesa.com/en-int/newsroom/2019/06/190612-siemens-gamesa-inauguration-energy-system-thermal`

[41] Wirtschaft und Energie, Bundesministerium für. Kohleausstieg und Strukturwandel. 16.08.2020. Available from: `https://www.bmwi.de/Redaktion/DE/Artikel/Wirtschaft/kohleausstieg-und-strukturwandel.html`

[42] The Engineer. Team connects first grid-scale pumped heat energy storage system. 2019. Available from: `https://www.theengineer.co.uk/grid-scale-pumped-heat-energy-storage/`

[43] The Northern Echo. New energy storage technology places the UK at the forefront of emerging global market. 2019. Available from: https://www.thenorthernecho.co.uk/business/17346467.new-energy-storage-technology-places-uk-forefront-emerging-global-market/

[44] Dumont, o.; Frate, G. F.; Pillai, A.; et al. Carnot battery technology: A state-of-the-art review. *Journal of Energy Storage*, volume 32, 2020: p. 101756, Doi: 10.1016/j.est.2020.101756.

[45] MAN Energy Solutions. A tale of fire and ice. 07.08.2020. Available from: https://www.man-es.com/discover/a-tale-of-fire-and-ice

[46] Modern Power Systems. MAN ETES: a cool technology that's heating up sector coupling. 2019. Available from: https://www.modernpowersystems.com/features/featureman-etes-a-cool-technology-thats-heating-up-sector-coupling-7314754/

[47] MAN Energy Solutions. MAN ETES: Electro-thermal energy storage. 2020. Available from: https://www.man-es.com/docs/default-source/energy-storage/etes/etes-energy-storage.pdf?sfvrsn=54340d66_4

[48] Morandin, M.; Mercangöz, M.; Hemrle, J.; et al. Thermoeconomic design optimization of a thermo-electric energy storage system based on transcritical CO2 cycles. *Energy*, volume 58, 2013: pp. 571–587, ISSN 03605442, Doi: 10.1016/j.energy.2013.05.038.

[49] A. Schrøder Pedersen; K. Engelbrecht; S. Soprani; et al. High-Temperature Thermal Energy Storage for electrification and district heating. *1st Latin American Conference on Sustainable Development of Energy, Water and Environment Systems*, 2018. Available from: https://orbit.dtu.dk/en/publications/high-temperature-thermal-energy-storage-for-electrification-and-d

[50] Marongiu, F.; Soprani, S.; Engelbrecht, K. Modeling of high temperature thermal energy storage in rock beds – Experimental comparison and parametric study. *Applied Thermal Engineering*, volume 163, 2019: p. 114355, ISSN 1359-4311, Doi: 10.1016/j.applthermaleng.2019.114355.

[51] Soprani, S.; Marongiu, F.; Christensen, L.; et al. Design and testing of a horizontal rock bed for high temperature thermal energy storage. *Applied Energy*, volume 251, 2019: p. 113345, ISSN 03062619, Doi: 10.1016/j.apenergy.2019.113345.

[52] Knobloch, K.; Muhammad, Y.; Costa, M. S.; et al. A partially underground rock bed thermal energy storage with a novel air flow configuration. *Applied Energy*, volume 315, 2022: p. 118931, ISSN 03062619, Doi: 10.1016/j.apenergy.2022.118931.

[53] Kai Knobloch; Thomas Ulrich; Christian Bahl; et al. Degradation of a Rock Bed Thermal Energy Storage System (in review). *Applied Thermal Engineering*, ISSN 1359-4311.

[54] Malta Inc. Our Story: Malta Inc. 2018. Available from: https://www.maltainc.com/our-story

[55] maltatoday. Codename 'Malta': Google owner Alphabet's secret lithium battery project. 13.07.2020. Available from: https://www.maltatoday.com.mt/business/technology/79406/codename_malta_google_owner_alphabets_secret_lithium_battery_project#.WxZCT5_7RhN

[56] Li, M.-J.; Zhu, H.-H.; Guo, J.-Q.; et al. The development technology and applications of supercritical CO2 power cycle in nuclear energy, solar energy and other energy industries. *Applied Thermal Engineering*, volume 126, 2017: pp. 255–275, ISSN 1359-4311, Doi: 10.1016/j.applthermaleng.2017.07.173.

[57] Geyer, M.; Freund, S. Webinar on Carnot Batteries: The Malta Carnot Batteries for "The Age of Storage". 2019. Available from: https://atainsights.com/wp-content/uploads/2019/04/190404-_Michael-Geyer-Sebastian-Freund-Webinar-Carnot-Batteries-distr.pdf

[58] Alva, G.; Liu, L.; Huang, X.; et al. Thermal energy storage materials and systems for solar energy applications. *Renewable and Sustainable Energy Reviews*, volume 68, 2017: pp. 693–706, ISSN 13640321, Doi: 10.1016/j.rser.2016.10.021.

[59] Benato, A.; Stoppato, A. Energy and cost analysis of an Air Cycle used as prime mover of a Thermal Electricity Storage. *Journal of Energy Storage*, volume 17, 2018: pp. 29–46, Doi: 10.1016/j.est.2018.02.007.

[60] Fernandez, A. I.; Martínez, M.; Segarra, M.; et al. Selection of materials with potential in sensible thermal energy storage. *Solar Energy Materials and Solar Cells*, volume 94, no. 10, 2010: pp. 1723–1729, ISSN 09270248, Doi: 10.1016/j.solmat.2010.05.035.

[61] Daschner, R.; Binder, S.; Mocker, M. Pebble bed regenerator and storage system for high temperature use. *Applied Energy*, volume 109, 2013: pp. 394–401, ISSN 03062619, Doi: 10.1016/j.apenergy.2012.10.062.

[62] Bindra, H.; Bueno, P.; Morris, J. F.; et al. Thermal analysis and exergy evaluation of packed bed thermal storage systems. *Applied Thermal Engineering*, volume 52, no. 2, 2013: pp. 255–263, ISSN 1359-4311, Doi: 10.1016/j.applthermaleng.2012.12.007.

[63] Shen, Y.-J.; Hou, X.; Yuan, J.-Q.; et al. Experimental Study on Temperature Change and Crack Expansion of High Temperature Granite under Different Cooling Shock Treatments. *Energies*, volume 12, no. 11, 2019: p. 2097, Doi: 10.3390/en12112097.

[64] Grosu, Y.; Faik, A.; Ortega-Fernández, I.; et al. Natural Magnetite for thermal energy storage: Excellent thermophysical properties, reversible latent heat transition and controlled thermal conductivity. *Solar Energy Materials and Solar Cells*, volume 161, 2017: pp. 170–176, ISSN 09270248, Doi: 10.1016/j.solmat.2016.12.006.

[65] Allen, K. G.; von Backström, T. W.; Kröger, D. G.; et al. Rock bed storage for solar thermal power plants: Rock characteristics, suitability, and availability. *Solar Energy Materials and Solar Cells*, volume 126, 2014: pp. 170–183, ISSN 09270248, Doi: 10.1016/j.solmat.2014.03.030.

[66] Anderson, R.; Bates, L.; Johnson, E.; et al. Packed bed thermal energy storage: A simplified experimentally validated model. *Journal of Energy Storage*, volume 4, 2015: pp. 14–23, Doi: 10.1016/j.est.2015.08.007.

[67] EUTIT. Cast basalt. 19.03.2021. Available from: `https://www.eutit.cz/clanky-cast-basalt.html`

[68] EUTIT. Cast basalt. 2010. Available from: `https://www.eutit.cz/clanky-cast-basalt.html`

[69] Engineering ToolBox. Water - Specific Heat. 2004. Available from: `https://www.engineeringtoolbox.com/specific-heat-capacity-water-d_660.html`

[70] Martin, R. T. Reference Chlorite Characterization for Chlorite Identification in Soil Clays. *Clays and Clay Minerals*, volume 3, no. 1, 1954: pp. 117–145, Doi: 10.1346/CCMN.1954.0030113.

[71] Blobel, V.; Lohrmann, E. Methode der kleinsten Quadrate. In *Statistische und numerische Methoden der Datenanalyse*, edited by V. Blobel; E. Lohrmann, Teubner-Studienbücher Physik, Stuttgart: Teubner, 1998, ISBN 978-3-519-03243-4, pp. 212–238.

[72] Materials Research and Building Chemistry — Katedra materiálového inženýrství a chemie, FSv, ČVUT v Praze. 27.01.2022. Available from: `https://k123.fsv.cvut.cz/materials-research-and-building-chemistry/`

[73] Kunii, D.; Levenspiel, O. *Fluidization engineering*. Butterworth-Heinemann series in chemical engineering, Boston: Butterworth-Heinemann, second edition, 1991, ISBN 0-409-90233-0.

Publications of the Author

[KR1] Rindt, K.; Hrdlička, F.; Novotný, V. Preliminary prospects of a Carnot-battery based on a supercritical CO2 Brayton cycle. *Acta Polytechnica*, volume 61, no. 5, 2021: pp. 644–660, ISSN 1210-2709, doi: 10.14311/AP.2021.61.0644.

[KR2] EERA JP EEIP (group of authors including Rindt, K.). Industrial Thermal Energy Storage - The Transition to a Sustainable CO2 Neutral Industry [in print]. 2022.

[KR3] Rindt, K., Pilař, L., Hrdlička, F. Speed Of Reaching The Full Potential Heat Capacity Of A Basalt Product: Experimental Results. *Proceedings of the International Renewable Energy Storage Conference 2021 (IRES 2021)*, 2022: pp. 136-142, ISSN 2589-4943, doi: 10.2991/ahe.k.220301.014.

[KR4] Edel, K., Pilař, L., Hrdlička, F. Thermodynamic Properties of Basalt and a Basalt Product for the Use in Energy Storage [Conference presentation]. *Conference STC 2021*, Prague, Czech Republic, 04.05.2021, Abstract available from: https://stc.fs.cvut.cz/history/2021/res_d1_en.pdf.

[KR5] Rindt, K., Pilař, L., Hrdlička, F. Speed of reaching the full potential heat capacity of a basalt product: Mathematical model based on experimental results [Paper presented at conference]. *ENERSTOCK 2021*, Ljubljana, Slovenia, 09.-11.06.2021: pp. 1-7, Abstract available from: https://www.enerstock2021.org/images/enerstock_2021_book_of_abstracts_FINAL_v2.pdf.

[KR6] Pavlíková, M.; Pivák, A.; Edel, K. and Pavlík, Z. High-Temperature Dilatometric Measurement of Basalt [Paper presented at conference]. *THERMOPHYSICS 2021*, Dalesice, Czech Republic, 07.-09.09.2021: pp. 1-5.